STAFF SUMMARY SHEET

	TO	ACTION	SIGNATURE (Surname), GRADE AND DATE		TO	ACTION	SIGNATURE (Surname), GRADE AND DATE
1	DFAN	sig	*Reed, Shad Lt Col 21July14*	6			
2	DFER	approve	*Soltz, AD27, 22July14*	7			
3	DFAN	action	(Author /Originator)	8			
4				9			
5				10			

SURNAME OF ACTION OFFICER AND GRADE	SYMBOL	PHONE	TYPIST'S INITIALS	SUSPENSE DATE
McLaughlin, Civ	DFAN	333-2613	tem	20140728

SUBJECT		DATE
Clearance for Material for Public Release USAFA-DF-PA- *384*		20140721

SUMMARY

1. PURPOSE. To provide security and policy review on the document at Tab 1 prior to release to the public.

2. BACKGROUND.
Authors: Timothy P. Jung, Ryan P. Starkey, Brian Argrow

Title: Modified Linear Theory F-function Applied to Numerical Prediction of Sonic Booms

Circle one: Abstract   Tech Report   Journal Article   Speech   Paper   Presentation   Poster
                 Thesis/Dissertation   Book   Other: _____

Check all that apply (For Communications Purposes):
        [] CRADA (Cooperative Research and Development Agreement) exists
        [] Photo/ Video Opportunities   [] STEM-outreach Related   [] New Invention/ Discovery/ Patent

Description: short description of the submission. Sonic boom pressure profiles calculated by modified linear theory are evaluated. These methods transform parametric description of aircraft into F-functions, which are used to predict the pressure profile after propagation through the atmosphere.

Release Information: To be submitted to the AIAA Journal of Aircraft for peer review and publication

Previous Clearance information: (If applicable): None

Recommended Distribution Statement: Distribution A: approved for public release, distribution unlimited

3. DISCUSSION.

4. RECOMMENDATION. Sign coord block above indicating document is suitable for public release. Suitability is based solely on the document being unclassified, not jeopardizing DoD interests, and accurately portraying official policy.

Thomas E. McLaughlin, Ph.D.
Director, Aeronautics Research Center

AF IMT 1768, 19840901, V5   PREVIOUS EDITION WILL BE USED.

Modified Linear Theory F-function Applied to Numerical Prediction of Sonic Booms

Timothy P. Jung [1] , Ryan P. Starkey [2] and Brian Argrow [3]
University of Colorado, Boulder, CO, 80309, USA

Sonic boom pressure profiles calculated by modified linear theory are evaluated. These methods transform parametric description of aircraft into F-functions, which are used to predict the pressure profile after propagation through the atmosphere. Although Whitham's F-function equation is the most widely used method, it cannot be applied to aircraft that have discontinuities in their area profiles. Thus, Lighthill's F-function is shown to be the best method. Procedures are presented to adapt Lighthill's method so it can be used for numerical calculation. Then, sonic boom pressure profiles from wind tunnel experiments, computational fluid dynamics, and flight tests are compared to profiles from Lightill's method to explore its accuracy. In general, Lighthill's modified linear theory method is able to predict the sonic boom shape, magnitude and duration within 10% and account for variations in lift, Mach number and propagation angle. The final case investigated is the XB-70. Its complex shape is not easily transformed into an axi-symmetric area profile, reducing the accuracy of the modified linear theory pressure profile. However, this study demonstrates that modified linear theory is a fast and sufficiently accurate to predict sonic booms and is appropriate for the preliminary and conceptual design stages of quiet sonic boom aircraft.

Nomenclature

c_D = drag coefficient

c_L = lift coefficient

[1] Associate Professor, Department of Aeronautics, 2354 Fairchild Drive, Headquarters, and AIAA Senior Member, timothy.jung@usafa.edu
[2] Assistant Professor, Aerospace Engineering Sciences, Campus Box 429, and AIAA Associate Fellow, rstarkey@colorado.edu
[3] Professor, Aerospace Engineering Sciences, Campus Box 429, and AIAA Associate Fellow, brian.argrow@colorado.edu

f = source strength

F = F-function, $\sqrt{\text{ft}}$

h = function in Lighthill's F-function

= propagation distance in vertical direction, ft

H = Heaviside step function

$ISPR$ = initial shock pressure rise, lb/ft^2

K_1 = Bessel function of second kind

$\mathcal{L}$ = length of aircraft, ft

L = lift, lbs

M = Mach number

p = Heaviside's operator

p_∞ = freestream static pressure, lb/ft^2

Δp = pressure perturbation, lb/ft^2

$\Delta \tilde{p}$ = non-dimensional pressure

q = dynamic pressure, lb/ft^2

r = radial coordinate, ft

R = radius of body of revolution, ft

S_V = cross-sectional area, ft^2

S_L = cumulative lift along x axis in units of area, ft^2

S_{eq} = total equivalent area, ft^2

u = velocity perturbation in x direction, ft/sec

v = velocity perturbation in r direction, ft/sec

$\mathcal{W}$ = weighting factor in F-function ft$^{-1/2}$

x = longitudinal coordinate from nose of aircraft, ft

$\tilde{x}$ = non-dimensional x distance

Δx = step size in x, y direction, ft

y = characteristic coordinate, ft

β = Prandtl-Glauert coefficient, $\sqrt{M^2 - 1}$

γ = ratio of specific heats

ζ = dummy variable of integration along y

μ = Mach angle, radians

χ = dummy argument

ϕ = velocity potential

      = propagation angle, degrees

Subscripts

eq = total equivalent area

f = fuselage

n = summation index

i = location i

L = Lighthill

ML = modified Lighthill

V = volume

W = Whitham

I. Introduction

The University of Colorado has used conceptual and preliminary design software named RapidF to design quiet sonic boom aircraft [1] and to investigate how to conduct scaled sonic boom tests in the atmosphere using Unmanned Aerial Systems [2]. Since RapidF is used as a conceptual design tool, it must be fast, and thus, lower fidelity; however, it must also be accurate so that the designer can properly evaluate a configuration. Therefore, modified linear theory was selected as the foundation of RapidF because it is capable of quickly and accurately predict far field pressure profiles. A pictorial representation of RapidF's flow is shown in Fig. 1. The program accepts design inputs and flight parameters. The most important inputs are are shown in Table 1. These values are transformed into an equivalent axi-symmetric area and lift profile along

3

the aircraft's longitudinal axis, as shown in the top of the RapidF box in Fig. 1. Then, using these area profiles, RapidF calculates the F-function using modified linear theory. Finally, RapidF sends the F-function to CUBoom which is a geometric acoustic propagation subroutine to predict the design's sonic boom pressure profile on the ground.

For brevity, the scope of this paper is limited to the F-function calculations and resultant pressure profiles. Thus, discussion concerning the methods used to generate the area profiles is abridged. A comprehensive description of RapidF's methodology can be found in Ref. [3]. The objectives of this paper are: 1) to determine the best F-function equation 2) specify how to use this equation, and 3) demonstrate that modified linear theory is as nearly as accurate as CFD in predicting a design's ground pressure profile, while taking significantly less time to execute.
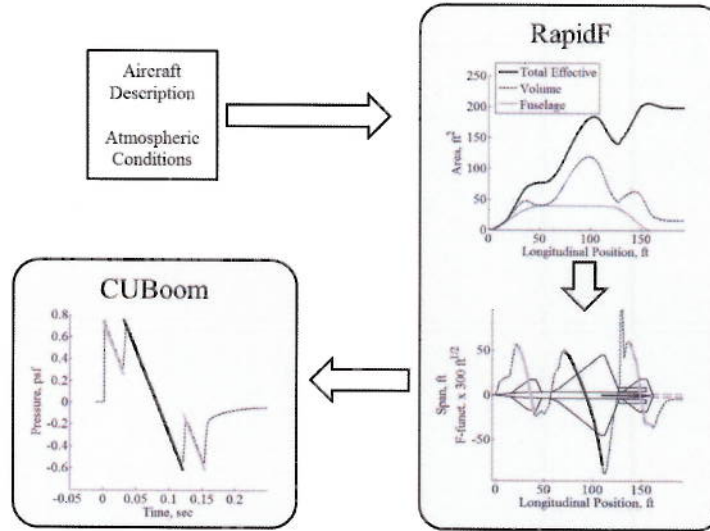
Fig. 1 Overview of RapidF.

II.   Modified Linear Theory

Modified linear theory is based on axi-symmetric linear theory, as the name implies. By limiting the flow to being above transonic but below hypersonic speed; and assuming a steady, irrotational and isentropic flow field with small perturbations, linear theory reduces the continuity, momentum and energy equations to a single equation with one variable, the velocity potential [4, 5]:

$$\frac{d^2\phi}{dr^2} + \frac{1}{r}\frac{d\phi}{dr} - \beta^2\frac{d^2\phi}{dx^2} = 0 \tag{1}$$

4

Table 1 Summary of inputs into RapidF software

Fuselage	Surfaces	Engine	Flight Conditions
Diameter	Location	Location	Mach number
Length	Leading edge sweeps (2)	Length	Angle of Attack
Diameter changes	Trailing edge sweeps (2)	Radius	Altitude
Nose type	Chord and span	Internal/external	Weight
Nose length	Airfoil shape	Pressure ratio	
Boat tail type	Incidence angle	% Spillage	
Boat tail length	Dihedral	Fuel Consumption	
	Twist	Thrust	

where the Prandtl-Glauert coefficient is:

$$\beta = \sqrt{M_\infty^2 - 1} = \frac{1}{\tan\mu} \qquad (2)$$

As shown in Fig. 2, the characteristics are linear of the form $y = x - \beta r$. Linear theory has been widely used to obtain first-order approximations of surface pressures and aerodynamic forces on aircraft and has consistently compared well to experimental data [6]. However, as presented above, it cannot predict the flow field far from a supersonic source, which is the location of concern for sonic boom minimization research, because the theory fails to account for non-linear effects.

Modified linear theory, pioneered by Whitham [7], adapted linear theory to be used away from the source. He used a potential defined by a source function, $f(x)$, along the x-axis as a solution to Eq. (1):

$$\phi = \int_0^{x-\beta r} \frac{-f(\zeta)}{\sqrt{(x-\zeta)^2 - \beta^2 r^2}} d\zeta \qquad (3)$$

The source strength is determined by the boundary conditions. As with any potential function, the velocity profile can be found by taking the derivative of Eq. (3) with respect to x and r. Whitham used an F-function:

$$F(y) = \int_0^y \frac{f'(\zeta)}{\sqrt{y-\zeta}} d\zeta \qquad (4)$$

to simplify calculations because the F-function remains constant along a characteristic and the flow properties
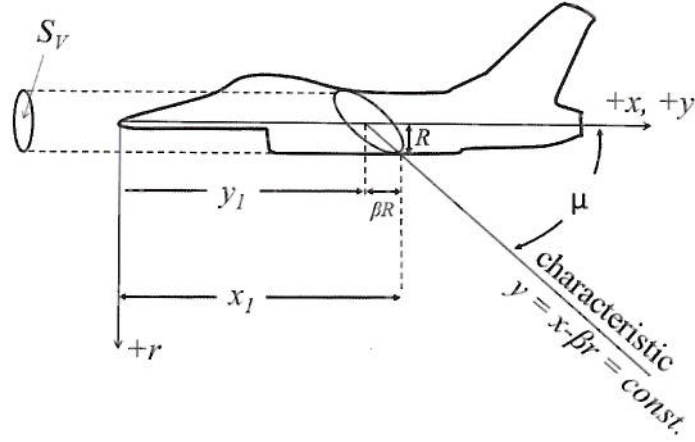
Fig. 2 Linear theory geometry.

can be easily calculated via:

$$u = \frac{d\phi}{dx} = -\frac{1}{\sqrt{2\beta r}}F(y) \tag{5}$$

$$v = \frac{d\phi}{dr} = \sqrt{\frac{\beta}{2r}}F(y) \tag{6}$$

$$\Delta p = \frac{\gamma p_\infty M_\infty^2}{\sqrt{2\beta r}}F(y) \tag{7}$$

In Eq. (4), the integration is conducted over y. As shown in Fig. 2, y_1 can be interpreted as the location on the x-axis where the characteristic caused by the radius change at x_1 starts. Thus, integration over y is in the x-direction, along the aircraft centerline. Once the F-function is calculated from Eq. (4), the complete flow field can be estimated from Eqs. (5–7). The velocities are only depended on the characteristic, y and radial distance, r. In general, as can be seen by inspecting Eqs. (5–7) the perturbations decrease as a function of $r^{-1/2}$. This also causes the perturbations to be infinite at the source, limiting modified linear theory to the region away from the source or near the nose where $\beta r \gg y$.

Equations (5–7) are not sufficient in of themselves to describe the far field, because variations in the local speed of sound will cause the characteristics to curve. Whitham modified the characteristics to include a non-linear term to allow them to bend [7]:

$$y = x - \beta r + \frac{(\gamma+1)M_\infty^4}{\sqrt{2\beta^3}}\sqrt{r}F(y) \tag{8}$$

6

The modified characteristics can be used to predict shock locations. As shown in Fig. 3, each characteristic curves at its own rate related to its F-function value, which allows characteristics to intersect. When two characteristics merge, a shock forms. This is an improvement from classical linear theory which cannot predict shock locations, even on the object's surface. By assuming the shocks are weak (small entropy change), the shock strength can be calculated from Eq. (7) in the form:

$$\frac{\Delta p}{p_\infty} = \frac{\gamma M^2}{\sqrt{2\beta r}} \left(F(y_2) - F(y_1) \right) \tag{9}$$

In summary, modified linear theory, as a subset of linear theory, has the same assumptions and restrictions. Its prediction of the flow properties is still first order, with the exception of the characteristics, which are higher order. This modest change enables modified linear theory to be used in the far field. The F-function is the key to modified linear theory because it has multiple applications. In Eqs. (5–7), it is used to describe the velocity and pressure perturbations and in Eq. (8), it describes the curvature of the characteristics, which predicts shock locations and strengths. For this reason modified linear theory is well suited for RapidF. When designing a quiet supersonic aircraft, the user is immediately aware of the component's impact on the F-function and thus, the sonic boom pressure profile as was demonstrated in Ref. [1].
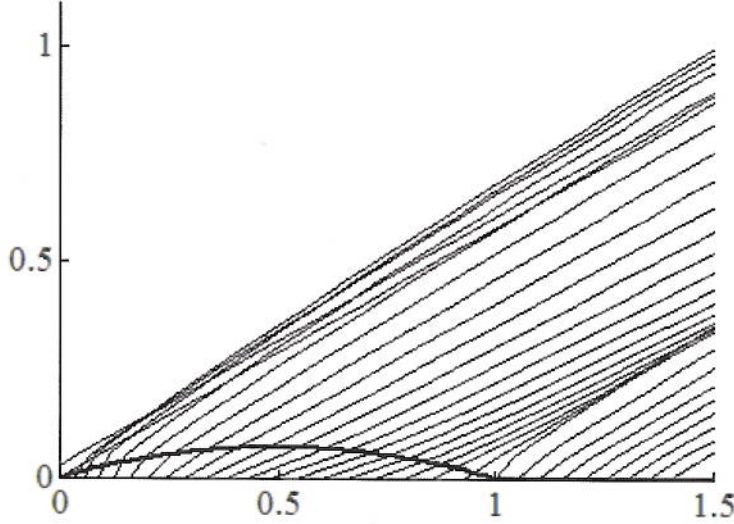

Fig. 3 Example of modified linear theory curved characteristics from an elliptical body.

A. Whitham's F-function

By using the flow tangency boundary condition, Whitham determined a method to calculate the F-function from the surface shape. The radial velocity can be found by taking the derivative of Eq. (3) with respect to r:

$$v = \frac{d\phi}{dr} = \frac{1}{r} \int_0^{x-\beta r} \frac{(x-\zeta)f'(\zeta)}{\sqrt{(x-\zeta)^2 - \beta^2 r^2}} d\zeta \tag{10}$$

Evaluating the above equation at the surface and assuming a slender body ($R \approx 0$):

$$v|_{body} = \frac{f(y)}{r} \tag{11}$$

Since the flow must be tangent to the body at the surface:

$$R' = \frac{v|_{body}}{1 + u|_{body}} \approx v|_{body} \tag{12}$$

Combining the above two equations, the source strength can be calculated from the surface geometry by:

$$f(y) = RR' \tag{13}$$

The cross sectional area, S_V, associated with R is:

$$S_V = \pi R^2 \tag{14}$$

and by differentiation:

$$S_V' = 2\pi RR' \tag{15}$$

Combining Eqs. (13) and (15):

$$f(y) = \frac{1}{2\pi} S_V' \tag{16}$$

Finally, by differentiation:

$$f'(y) = \frac{1}{2\pi} S_V''(x) \tag{17}$$

which can be substituted into Eq. (4) to provides a method for calculating the F-function:

$$F(y) = \int_0^y \frac{S_V''(\zeta)}{\sqrt{y-\zeta}} d\zeta \tag{18}$$

8

Equation (18) will be referred to hereafter as Whitham's F-function equation. Results from this equation can be used in Eqs. (5–7) to describe the flow field. However, it requires S'_V and S''_V to be continuous.

Whitham initially limited his theory to axi-symmetric, non-lifting objects. Later, he [8] and Walkden [9] expanded the theory to include non-axi-symmetric and lifting surfaces, respectfully, which were experimentally validated by Carlson [10]. In general, these researchers added the equivalent area due to lift to the equivalent area from volume to produce the total equivalent area:

$$S_{eq}(y) = S_L(y) + S_V(y) \tag{19}$$

where the area due to lift, S_L, is the cumulative lift in units of area:

$$S_L(y) = \frac{\beta \cos \phi}{2q} \int_0^y L(\zeta)d\zeta \tag{20}$$

The total equivalent area (referred to as total area for brevity), $S_{eq}(y)$, is the sum of the two areas and is used in Eq. (18) to calculate the F-function. Thus, Whitham's F-function can be used on a non-axi-symmetric body producing lift.

To find the F-function, using Whitham's F-function at location y, the second derivative at all locations ζ in front of y are weighted by:

$$\mathcal{W}_W(\zeta) = \frac{1}{\sqrt{y - \zeta}} \tag{21}$$

Based on this weighting, one can interpret Eq. (18) as stating that the F-function is mostly a function of the local curvature. The curvature of locations in front of the point of interest do influence the F-function; however, the influence rapidly decreases as the distance between the points increases. For example, Fig. 4(b) compares the local first and second derivative to the F-function of a low sonic boom aircraft from Ref. [1]. Since, Whitham's F-function integrates the second derivative, the first derivative follows the F-functions trends; thus, the first derivative can be used as a crude approximation of the F-function. This is consistent with supersonic linear theory where the surface pressure is only a function of the local surface inclination and that information cannot be transmitted upstream. However, Fig. 4 highlight's a problem when using Whitham's F-function on an aircraft. Whitham's F-function equation requires S'' to be continuous. Although aircraft are usually smooth to minimize drag, discontinuities do exist in the cross-sectional area profile, such as the engine inlets, as shown in Fig. 4(a). Whitham's F-function in Fig. 4(c) shows a large spike in the F-function at this location. These spikes are sensitive to grid density as will be shown later.
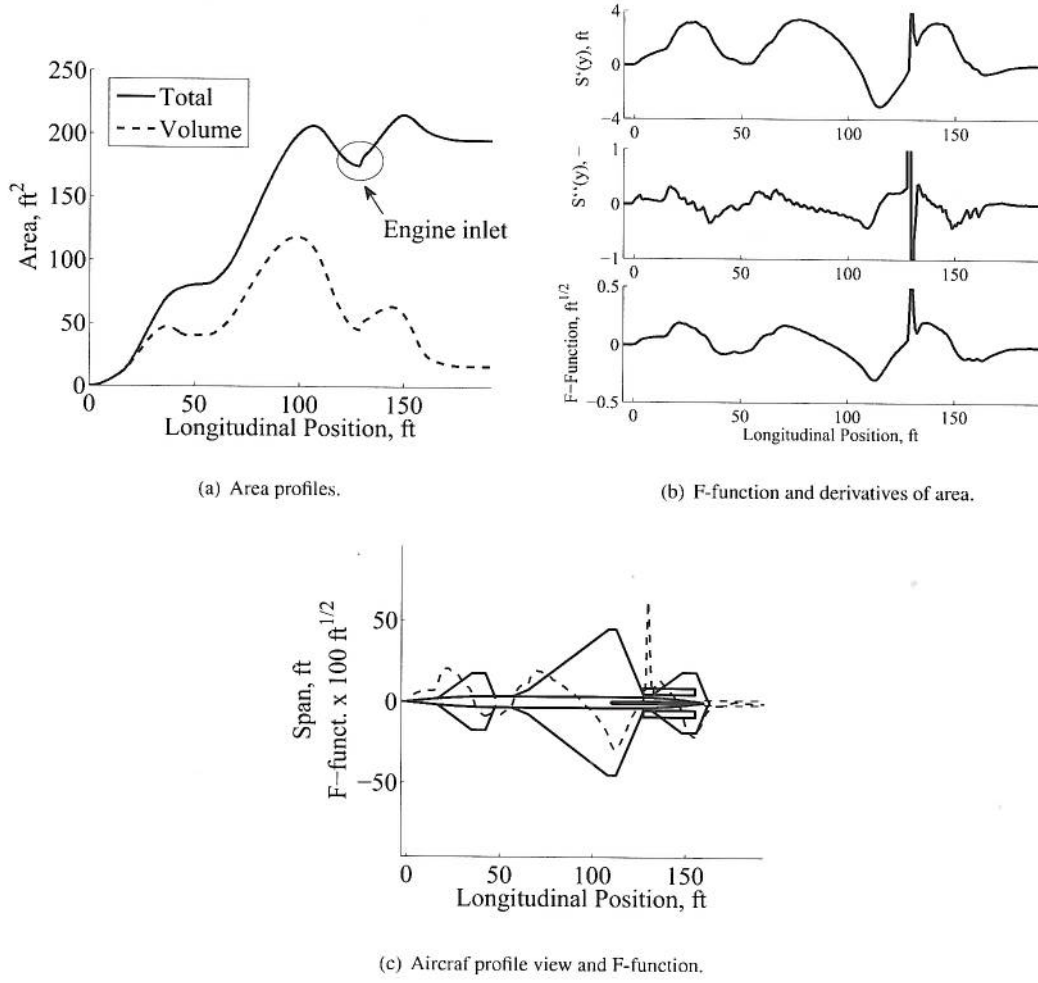
(a) Area profiles.

(b) F-function and derivatives of area.

(c) Aircraf profile view and F-function.

Fig. 4 Area profiles, derivatives, and Whitham's F-function of an aircraft.

To use Whitham's equation, in RapidF, it must be discretized to allow numerical integration. Using a second order estimate of the second derivative of the area, Eq. (4) becomes:

$$F_i = \frac{1}{2\pi} \sum_{n=1}^{i-1} \left(\frac{S_{n-1} - 2S_n + S_{n+1}}{(\Delta x)^2} \frac{1}{\sqrt{x_i - x_n}} \right) \Delta x \tag{22}$$

Integration cannot include $n = i$ because the last term would be infinite. For the last term in the summation, $n = i - 1$; thus, $x_i - x_n = \Delta x$ and the term simplifies to:

$$\frac{1}{2\pi} \left(S_{i-2} - 2S_{i-1} + S_i \right) \Delta x^{-3/2} \tag{23}$$

Thus, as the user increases the grid density, decreasing Δx, the weight on this last point increases, making Whitham's equation sensitive to grid density. Because of this issue, combined with the inability to account for discontinuities, a more robust equation was sought for RapidF.

10

B. Stieltjes F-function

One method to calculate an F-function with discontinuities is to use a Stieltjes integral of the general form [11]:

$$\int P(x)dG(x) = \int P(x)G'(x)dx \tag{24}$$

Thus, Whitham's F-function can be calculated by [5]:

$$F(y) = \frac{1}{2\pi} \int_0^y \frac{dS'(\zeta)}{\sqrt{y - \zeta}} \tag{25}$$

This equation will be referred to as the Stieltjes' F-function. It still requires a correction for where $S'(\zeta)$ is discontinuous. According to Whitham [7], this correction is:

$$\Delta F(y)_i = \frac{1}{2\pi} \sqrt{\frac{2}{\beta R_i}} \Delta S'_i \tag{26}$$

which is essentially the same as Lighthill's F-function (discussed in the next section). The above equations can be applied in the following manner: Equation (25) is used to calculate the F-function up to a discontinuity in $S'(\zeta)$, then Eq. (26) is used to calculate the F-function jump at the discontinuity. Then, Eq. (25) is used again until the next discontinuity. The process is repeated until reaching the end of the aircraft. However, Eq. (25) must be calculated numerically. To do so, dS' at point n is:

$$\begin{aligned}
dS'_n &= S'_{forward} - S'_{backwards} \\
&= \frac{S_{n+1} - S_n}{\Delta x} - \frac{S_n - S_{n-1}}{\Delta x} \\
&= \frac{S_{n-1} - 2S_n + S_{n+1}}{\Delta x}
\end{aligned}$$

Substituting this into Eq. (25) and discretizing:

$$F_i = \frac{1}{2\pi} \sum_{n=1}^{i} \left(\frac{S_{n-1} - 2S_n + S_{n+1}}{\Delta x} \frac{1}{\sqrt{x_i - x_n}} \right) \tag{27}$$

This is numerically the same as Eq. (22) and there is no advantage of the Stieltjes integral compared to Whitham's F-function. For example, an F-function calculated from Eq. (25) is compared to one from Whitham's Function, Eq. (18), in Fig. 5. As expected, they are identical. The Stieltjes F-function had to be offset vertical because the F-functions are virtually the same. This observation has been previously stated by Ritzel and Gottlieb in Ref. [5]. Therefore, the Stieltjes F-function equation was not pursued as a viable choice for RapidF.
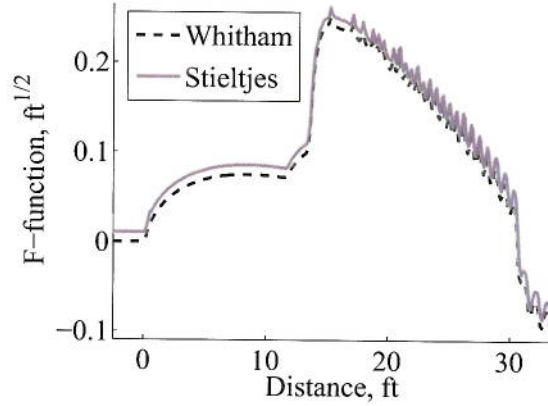
11

Fig. 5 Whitham's and Stieltjes' F-functions (Stieltjes offset by 0.1 ft$^{1/2}$).

C. Lighthill's F-function

In his 1952 paper [7], Whitham built on Lighthill's linear theory for bodies with slope discontinuities [12] to develop an alternative to Eq. (18):

$$F(y) = \int_0^\infty \sqrt{\frac{2}{\beta R(\zeta)}} \quad h\left(\frac{y-\zeta}{\beta R(\zeta)}\right) \frac{dS'(\zeta)}{2\pi} \tag{28}$$

The above equation will be referred to as Lighthill's F-function, where:

$$h(\chi) = \sqrt{\frac{\pi}{2p}} \frac{1}{K_1(p)} H(\chi) \tag{29}$$

Here p is the Heaviside operator for differentiation, K_1 is the Bessel function of second kind, and $H(\chi)$ is a step function. The derivation of Lighthill's F-function did not require the assumption of a smooth area profile as was in Whitham's and Stieltjes' F-functions. This is a significant improvement, which allows Lighthill's F-function to be applied to objects that have discontinuities. For example, a comparison of Whitham and Lighthill methods is shown in Fig. 6 for a nose cone to fuselage joint with a 3.2^o change in flow angle. Although the discontinuity is small, Whitham predicts a large expansion. This example demonstrates that even a small discontinuity has significant effect on Whitham's F-function. Since a digitized representation of an aircraft's area profile has a finite jump at each grid point as shown in Fig. 7, any numerical area profile effectively has a discontinuity at every location and Lighthill's method appears better suited for calculating an aircraft F-function using numerical integration.

The only difference between Lighthill's and Whitham's F-functions is the weighting. Since Lighthill's equation, Eq. (28), is also a Stieltjes integral, his uses of $dS'(\zeta)$ is equivalent to Whitham's $S''(\zeta)d\zeta$. There-

12

fore, the large disparity in the F-functions shown in Fig. 6 is not caused by Whitham's use of $S''(\zeta)$, but by his weighting. Based on Eq. (28), Lightill's F-function weighs each point by:

$$W_L(\zeta) = \sqrt{\frac{2}{\beta R(\zeta)}} h\left(\frac{y-\zeta}{\beta R(\zeta)}\right) \tag{30}$$

The $h(\chi)$ function, Eq. (29), is plotted in Fig. 8. When $\chi < -1$, then $h(\chi) = 0$; when $\chi = -1$, then $h(\chi) = 1$; and when χ is large, $h(\chi) \approx (2\chi)^{-1/2}$, and the weight simplifies to:

$$W_L \approx \sqrt{\frac{2}{\beta R(\zeta)}} \sqrt{\frac{\beta R(\zeta)}{2(y-\zeta)}} \approx \frac{1}{\sqrt{y-\zeta}} \tag{31}$$

and comparing this to Eq. (21), Whitham's and Lighthill's weighting are the same. Their weights are only significantly different where $(y-\zeta)/(\beta R(\zeta))$ is small, near y, as shown in Fig. 9. This figure demonstrates
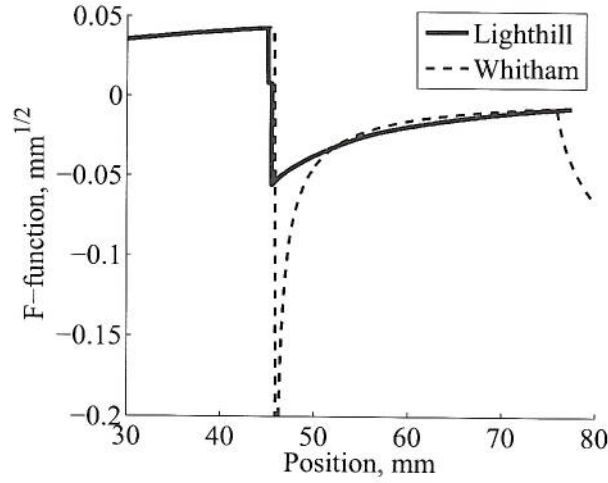
Fig. 6 Comparison of Whitham and Lighthill F-functions at a discontinuity. [5].

(a) Smooth or continuous.
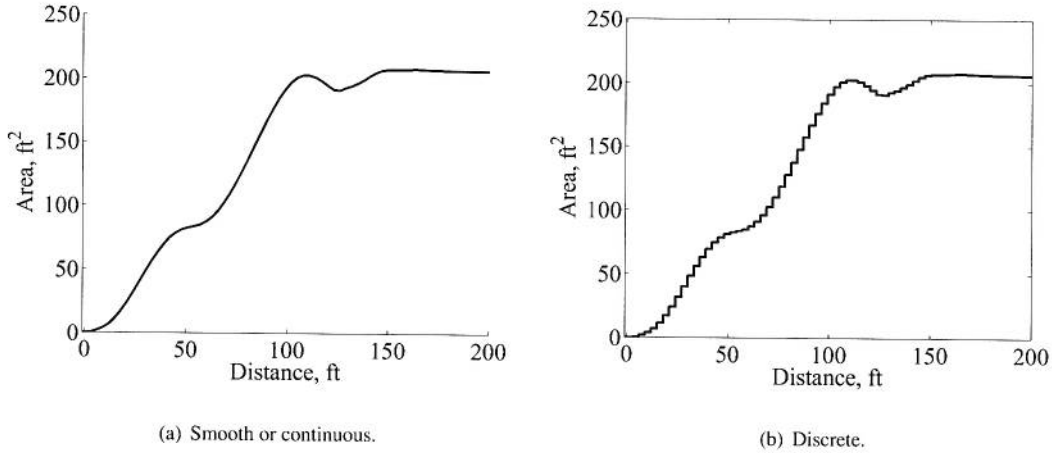
(b) Discrete.

Fig. 7 Smooth and discrete total equivalent area profiles.

13
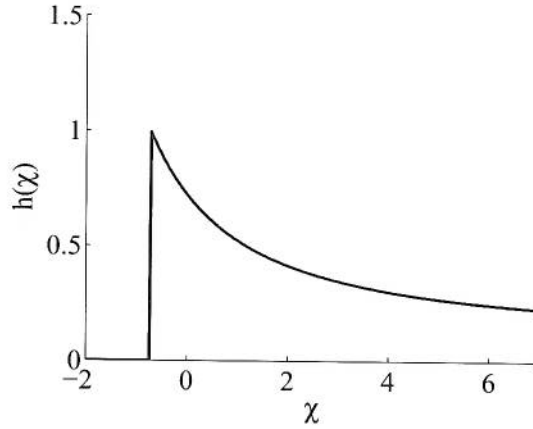
Fig. 8 The $h(\chi)$ function.
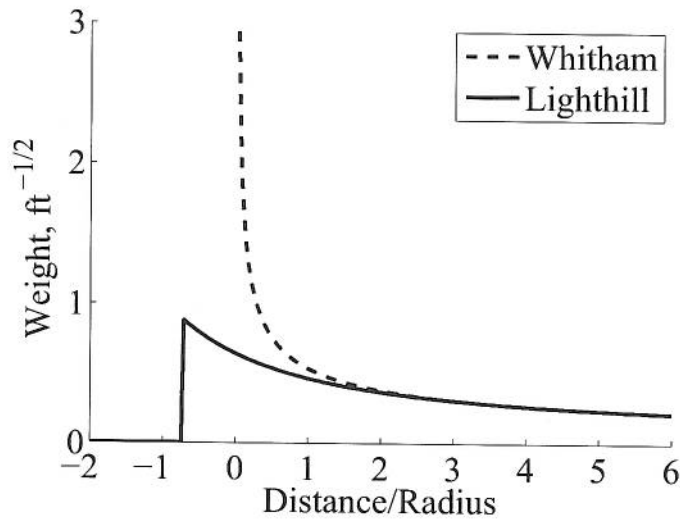
Fig. 9 Whitham and Lighthill weighting.

that at large distances Whitham's and Lighthill's weighting are the same as suggested by Eq. (31). It is also important to note that the area under each curve is equal.

Lighthill's F-function has not been widely implemented due to the difficulty in implementing Heaviside calculus and Bessel functions. In the 1980s, Gottlieb and Ritzel compared Whitham's and Lighthill's methods to projectiles with discontinuities [5, 13]. They found that Whitham's theory poorly predicted the F-function at discontinuities, which should have been anticipated since a discontinuity violates the smooth assumption. One drawback of using Lighthill's method is a higher computational cost. In order to speed processing time, Gottlieb and Ritzel proposed using a modified method where Whitham's equation is used

14

in regions with a smooth area profile and adding a correction at discontinuities based on Lighthill's equation. Initially, this method was attempted in this study, but was difficult to implement since it requires logic to find discontinuities. Furthermore, every location is essentially a discontinuity when doing numerical integration, as was shown in Fig. 7(b). Although Lighthill's F-function is valid at every point, Gottlieb and Ritzel were hesitant to solely use Lighthill's equation because of computation time and advocated for the Stieltjes method discussed earlier. In the 20+ years since their papers were published, advances in computers have made this argument irrelevant. Thus, for this study a method was developed to implement Eq. (28) at every location for aircraft designs.

Lighthill's method is more computationally expensive than Whitham's because Eq. (29) is time consuming to calculate. Previously, this cost was avoided by approximating $h(\chi)$ as $(2\chi)^{-1/2}$. However, if this approximation is used, Eq. (28) simplifies to Eq. (18) and any advantage in using Lighthill's method is lost. Thus, in order to improve accuracy and computational speed a look-up table was created for $h(\chi)$, as suggested by Gottlieb and Ritzel [5]. This allows Lighthill's method to be used accurately and with no speed penalty.

Lighthill's equation has never been applied to an aircraft, only to axi-symmetric, non-lifting objects; therefore, some adaptations needed to be made for use in RapidF. First, the total equivalent area (lift and volume) from Eq. (19), is used to calculate $dS'(\zeta)$ based on Walkden work that concluded lift could be replaced by an equivalent area defined in Eq. (20) [9].

Next, the domain of influence needed to be modified. In Whitham's F-function, the domain of influence is limited by the limits of integration. However, since the limits of Lighthill's equation are zero to infinity, the domain of influence is controlled in the h function in Eq. (30). The $\beta R(\zeta)$ in the denominator of the input to the h function has significant effect on the calculations, which is shown pictorially in Fig. 10. As seen in Eq. (30), the $\beta R(\zeta)$ term provides a method to non-dimensionalize $y - \zeta$ and also determines at what $y - \zeta$ value the $h(\chi)$ is zero, due to the step function. In other words, the $\beta R(\zeta)$ controls how far beyond point y, the aircraft's shape contributes to the F-function at point y, as shown in Fig. 10(b). If $R(\zeta)$ is approximated as $R(y)$, then the domain of influence is as shown in Fig. 10(c), which is consistent with linear theory: a radius change at $y + \beta R$ act as if it began at the centerline at y.

RapidF slices the aircraft at the Mach angle and projects the area along characteristics back to centerline

15

(a) Points in front of y.

(b) Points after y.

(c) Domain of influence assuming $R(\zeta) \approx R(y)$.
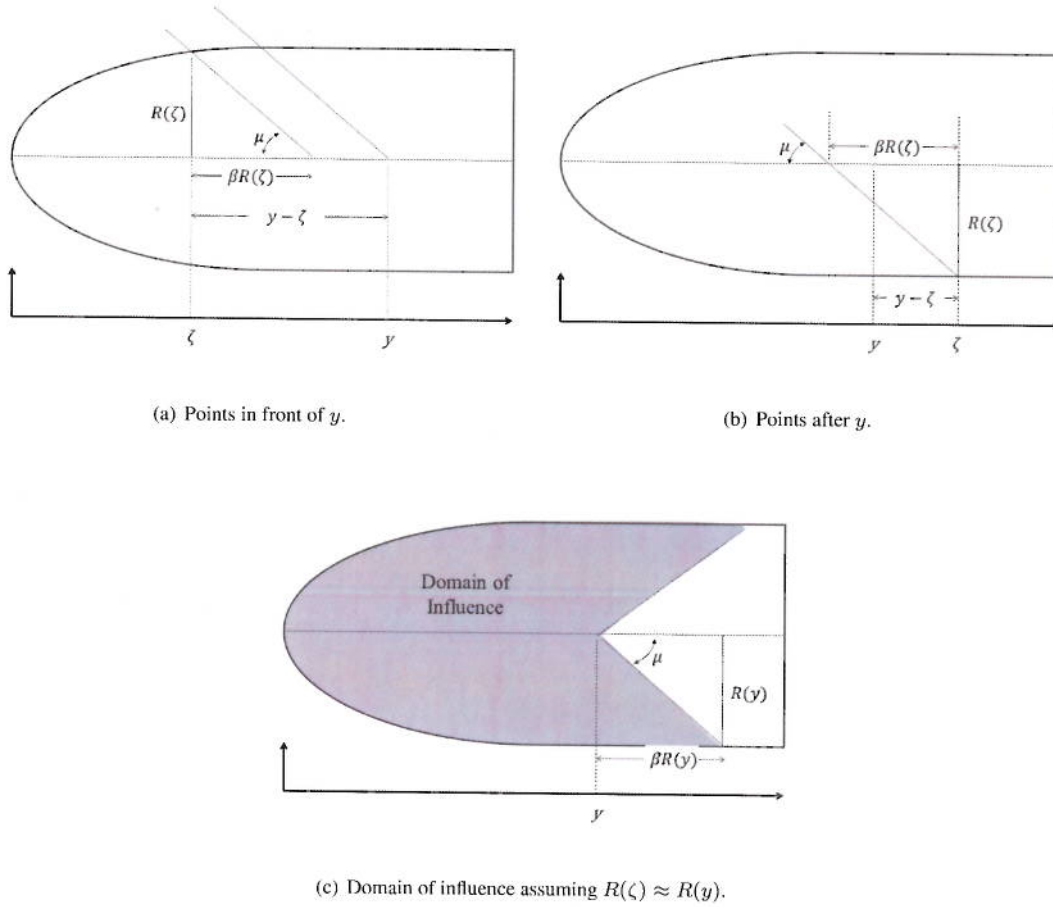
Fig. 10 Lighthill's weighting.

as was shown in Fig. 2. For example, refer to the engine shown in Fig. 11(a). It is located at 127 ft from the aircraft nose and is 7 ft below the aircraft. If the aircraft is flying at Mach 1.7, then the area increase from the engine acts as if it emanates from 117.6 ft along the centerline. Thus, the area profile from the engine is shown in Fig. 11(b). In Fig. 11(c), the Lighthill F-function from this area profile is shown compared to Whitham's F-function. Because Lighthill's domain of influence extends past the point of interest, as was shown in Fig. 10(c), the engine effects in the Lighthill's F-function begin at approximately 111 ft, where $(111 - 117.6)/(\beta R(\zeta)) = -1$. This is an an undesirable attribute of Lighthill's method because the engine should influence the F-function at 117.6 ft. In RapidF, since the aircraft has already been sliced at the Mach angle, as shown in Fig. 2, the equivalent area at point y_1 includes the effects of the area and lift at $x_1 + \beta R$. Thus, when RapidF calculates the total equivalent area, it has already projected it back to the aircraft centerline, consistent with the domain of influence shown in Fig. 10(c). To avoid shifting the engine

(a) Geometry of the engine.

(b) Engine area profile.

(c) F-functions.
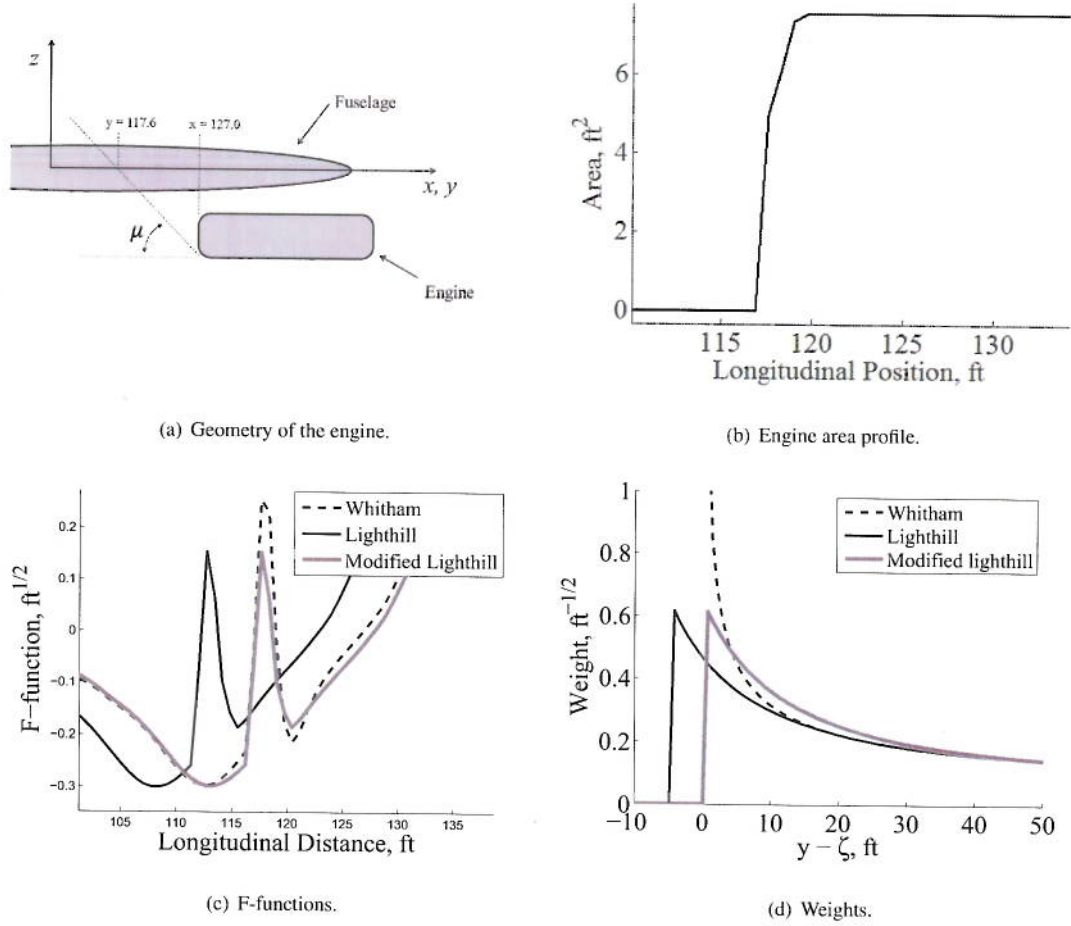
(d) Weights.

Fig. 11 Engine example.

area forward a second time, Lighthill's weighting is modified:

$$
\mathcal{W}_{ML}(\zeta) = \sqrt{\frac{2}{\beta R(y)}} h\left(\frac{y-\zeta}{\beta R(y)} - 1\right)
\tag{32}
$$

as shown in Fig. 11(d), with the corresponding F-function shown in Fig. 11(c). This allows features in the F-function to appear at the appropriate location in the F-function, while keeping the area under the weighting curves in Fig. 11(d) constant.

Finally, a value was need to be used for $R(\zeta)$. As already explained, the $\beta R(\zeta)$ term affects the effective domain of influence. Several values were explored to include:

- $R_{eq}(\zeta) = \sqrt{S_{eq}/\pi}$: Total equivalent area (lift and volume), in units of length

- $R_V(\zeta) = \sqrt{S_V/\pi}$: Equivalent area of volume, in units of length

- $R_f(\zeta)$: Local fuselage radius

17

The first two radii choices were significantly larger than the fuselage radius and shifted the effect of aircraft components too early in the F-function. Thus, the radius used in RapidF is the fuselage radius. However, it is possible to have components such as highly swept wings and horizontal tails to extend past the fuselage. In these cases $R_f(\zeta) = 0$, causing a divide by zero problem in Eq. (30). This is avoided by setting the minimum $R_f(\zeta)$ value to $0.02R_{f,max}$. All of the above modifications to Lighthill's F-function result in:

$$F(y) = \int_0^y \sqrt{\frac{2}{\beta R_f(\zeta)}} \quad h\left(\frac{y-\zeta}{\beta R_f(\zeta)} - 1\right) \frac{dS'_{eq}(\zeta)}{2\pi} \tag{33}$$

This equation will be referred to as the modified Lighthill's F-function equation.

D. F-function sensitivity

A grid sensitivity and convergence study was conducted on the classical Whitham method, Eq. (18), and the modified Lighthill method, Eq. (33). The primary input to the resolution of the RapidF solution is the user defined input distance between the slices along the aircraft centerline, Δx. However, the discussion below presents results using the "Number of Points'" or grid size, which is the aircraft length divided by Δx.

F-functions for various grid densities are shown in Fig. 12. The F-functions calculated using Whitham's method continue to distort as the grid is refined because the denominator in Eq. (18) is effected by Δx, as was shown in Eq. (23). Zoomed-in F-functions near the front of the aircraft which includes the canard are shown in Fig. 12(c) and 12(d). Whitham's method shows small oscillations or "scallops." These features are caused by the grid used to calculate the canard's area and lift not being aligned with the canard's leading and trailing edges as shown in Fig. 13. This misalignment causes the area profile to be stepped; creating a series of positive to negative second derivatives. Although the modified Lighthill method uses the same stepped area profile, the oscillations in the F-function are less severe because of the lighter weight given to these points close to the location of interest. Also, Whitham's method predicts a large F-function from the engine inlet, as shown in Fig. 12(e). The size of this feature increases with increasing number of points. In contrast, modified Lighthill's method is much less sensitive to these perturbations. Figure 14 shows the ground pressure profiles associated with the F-functions presented in Fig. 12. Whitham's method reasonably matches the modified Lighthill's method despite the oscillations associated with the lifting surfaces and the engines. This is because these spikes are like delta functions and contain very little acoustical energy and quickly dissipate with distance.

18

The results of these tests are summarized in Fig. 15. Figure 15(a) shows the maximum F-function value for each grid size. Whitham's method did not show F-function convergence and validated the analysis of the previous section that concluded modified Lighthill's method is the preferred method to be used for aircraft F-function calculations in RapidF. A dashed vertical line at 320 points is drawn in the graphs of Fig. 15 which is the lowest number of points used in this study. In Fig. 15(b), the maximum pressure value after propagation to the ground is shown. The modified Lighthill's method maximum pressure remains relatively constant after 320 grid points. Although Whitham's maximum pressure was also flat after 320 points, it was about 5% lower than modified Lighthill's pressure. Finally, the run times for each grid density is shown in Fig. 15(c) on a PC computer with a quad core AMD 640 II processor and 12 GB of memory. Both F-functions were calculated simultaneously during a single run; thus both methods have the same run times. The selection of 320 points allowed: run times to be less than one minute; the maximum F-function to be with 3.2% of the value using 1,600 points; and produced essentially the same ground pressure profile as predicted using higher grid density.
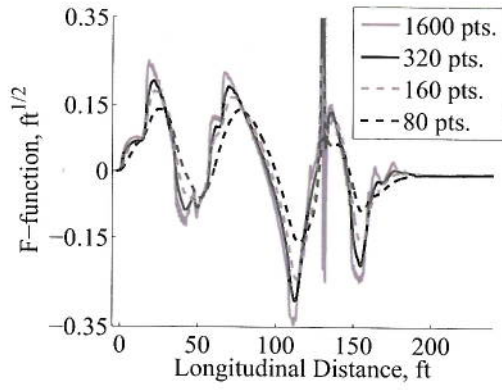
(a) Whitham's F-function.
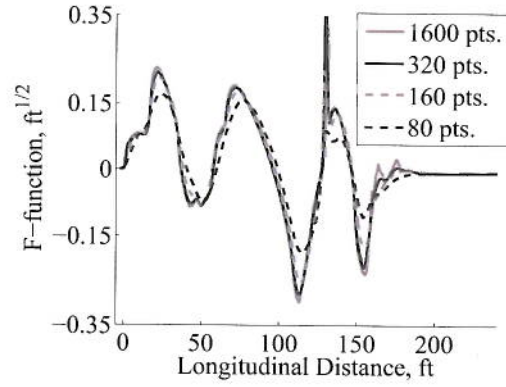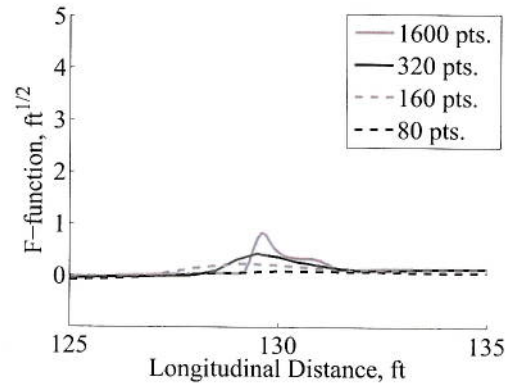
(b) Modified Lighthill's F-function.
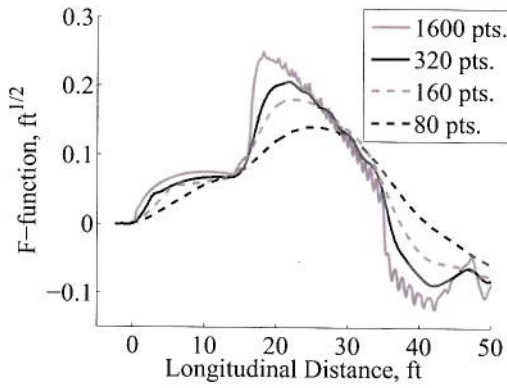
(c) Whitham's F-function near nose.
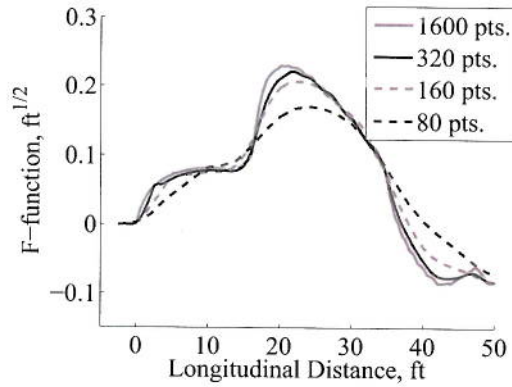
(d) Modified Lighthill's F-function near nose.
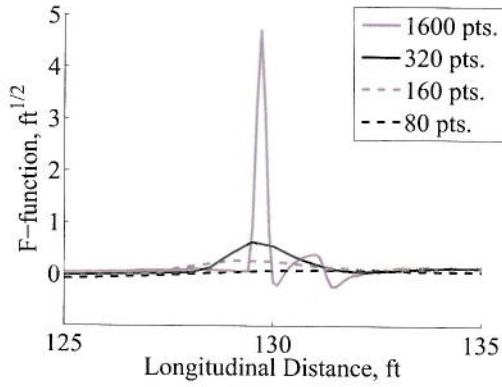
(e) Whitham's F-function at engine inlet.

(f) Modified Lighthill's F-function at engine inlet.
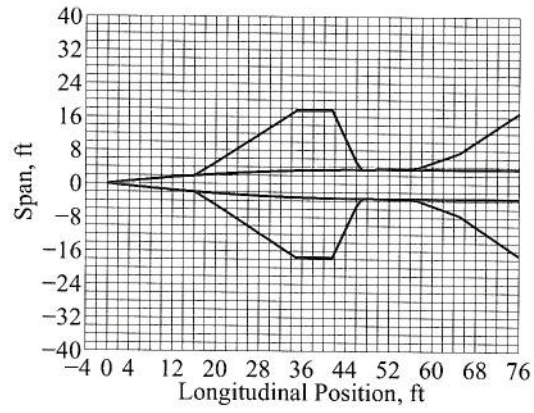
Fig. 12 F-functions for various grid densities.

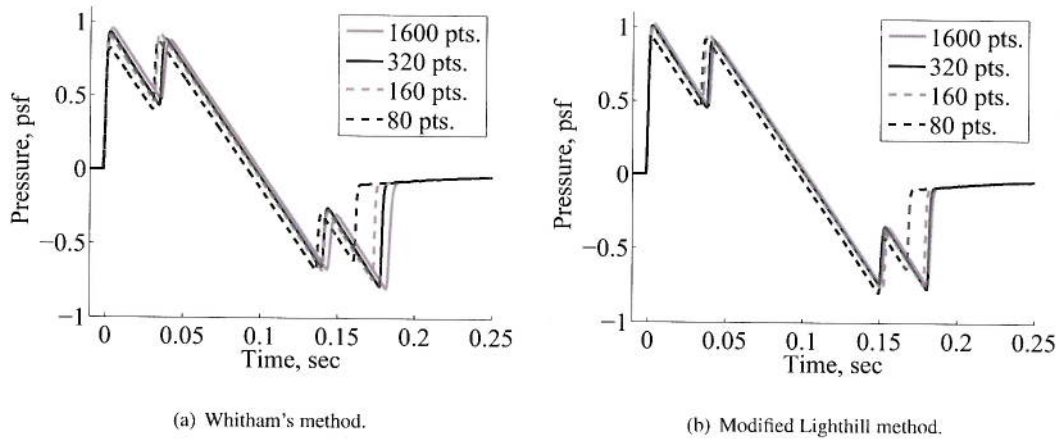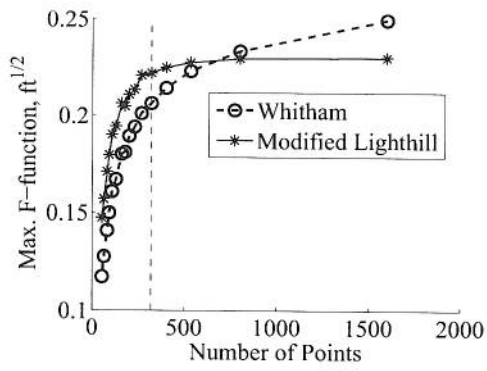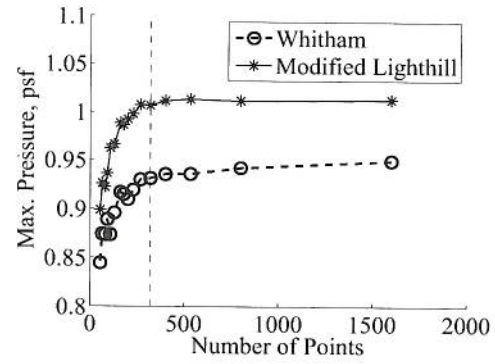Fig. 13 Grid used to obtain canard lift and volume distribution.

(a) Whitham's method.

(b) Modified Lighthill method.

Fig. 14 Ground pressure profiles for various grid densities.

(a) F-function.

(b) Ground pressures.
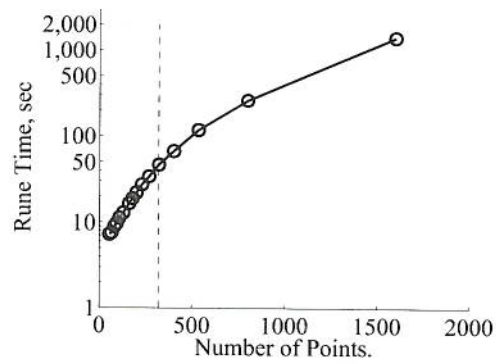
(c) Run times.

Fig. 15 Performance metrics for various grid densities.

III. RapidF Sonic Boom Pressure Profiles

In this section, sonic booms from RapidF are compared to historical results including legacy software based on modified linear theory, wind tunnel experiments, and flight test results. Since RapidF is based on a first order theory, it was known prior to this research that it is not the most accurate software available. The purpose of this section is to demonstrate that RapidF is sufficiently accurate, defined as within 10% of experimental results. More specifically RapidF's sonic booms should have:

1. The proper shape; RapidF's sonic boom should have the correct number of shocks and the shocks should be within 10% of the experimental location

2. Minimum and maximum pressures within 10% of the experimental results

3. Signal length should be within 10% of the experimental signal length

This section shows that, although it is low fidelity, based on first order theory, RapidF is able to accurately replicate sonic booms. Although RapidF occasionally does not meet the above criteria; overall, it consistently creates the correct shaped sonic boom and can be trusted to predict the sonic boom of conceptual designs.

A. Comparison of RapidF to Wind Tunnel Results

For an initial demonstration of RapidF's capabilities, pressure profiles were compared to wind tunnel experiments. Unlike sonic booms from flight tests, wind tunnel studies take place in a more controlled environment, mitigating the effects of atmospheric variables such as humility, winds, and turbulence; thus, making results more repeatable. NASA TM X-1236 [10], authored by Carlson, McLean and Shrout in 1966, was selected for this purpose. Despite its age, the report has many desirable traits. First of all, it presents a complete geometric description of the wind tunnel model, allowing implementation in RapidF with minimal assumptions. Second, it presents results for a variety of test conditions:

- Configuration: with and without nacelles, and two fuselage shapes
- Speed: $M = 1.41$ and 2.0
- Lift: $C_L = 0.0$, 0.1, and 0.2
- Propagation angle: $\phi = 0$, 45, 90 and 180°
- Propagation distance: 2.5, 5.0 and 10.0 body lengths away

Furthermore, it provided both experimental and theoretical results, allowing verification by comparing RapidF's output to the theoretical data and validation by comparing to the experimental results.

A drawing of the model used in the NASA TM X-1236 wind tunnel test can be seen in Fig 16, with dimension in centimeters. The model's engines were solid bodies of revolution with radii determined by subtracting the inlet capture area from the engine nacelle geometry. RapidF's model is depicted in Fig. 17. There are some minor differences compared to the model used in the wind tunnel tests. RapidF used one engine on the centerline with the same area profile of all four of the wind tunnel model's engines. This should not cause any errors for propagations directly beneath or above the aircraft, but might cause some disparities for side propagations as shown in Fig. 18. For simplicity only two engines are shown in this figure. When the aircraft with horizontally displaced engines is sliced at the Mach angle, each engine can create an its own area distribution. Thus, the simplified engine on RapidF's model might cause some errors for side propagation. Finally, the fillet where the wing trailing edge meets the fuselage is not modeled in RapidF.

Like RapidF, the NASA TM X-1236's theoretical pressure distribution was calculated using modified linear theory. The area profile was calculated by slicing the aircraft at the Mach angle, corrected for angle of attack by adapting a code designed for wave drag calculations [14]. This code divided components into a maximum of 30 slices, then estimated the area at each location to include the boundary layer displacement thickness. The lift distribution was calculated to include the nacelle to wing interference effects. The lift
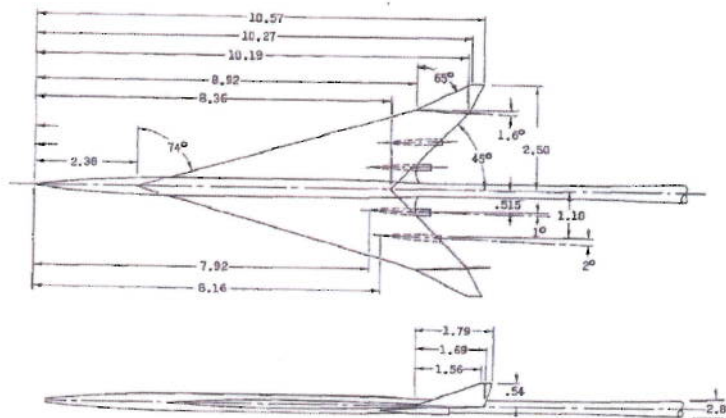

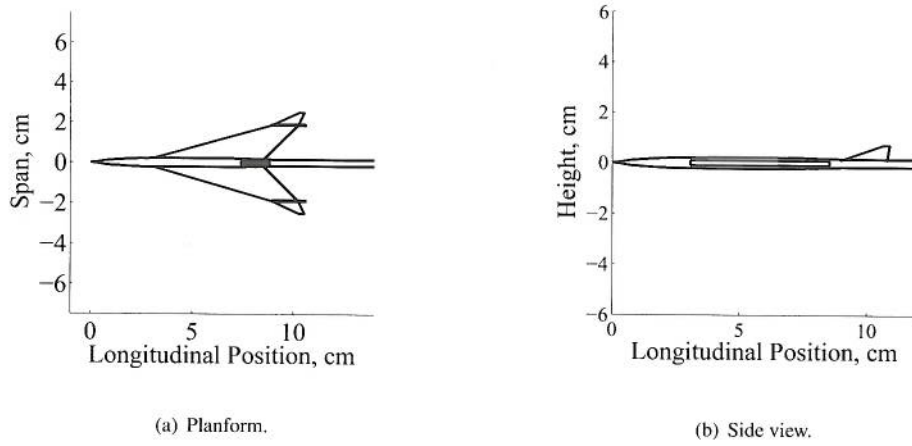**Fig. 16 Drawing of wind tunnel model (reproduced from NASA TM X-1236 [10]).**

24

(a) Planform.

(b) Side view.

Fig. 17 RapidF's representation of wind tunnel model used in NASA TM X-1236 [10].

Single engine on centerline

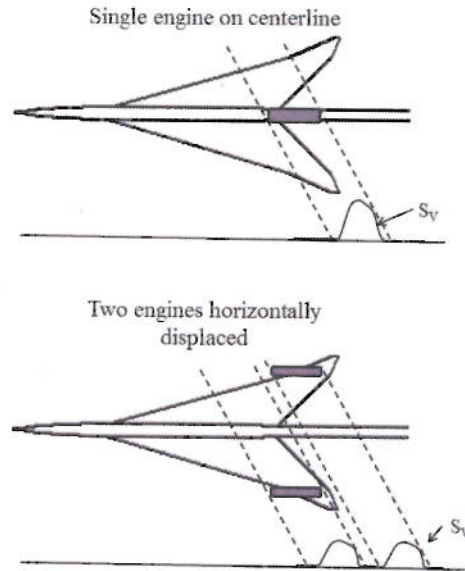Two engines horizontally displaced

Fig. 18 Area distributions of one versus two engines when propagating to the side.

profile was converted to an equivalent area via Eq. (20). Then, using the total area distribution, the F-function was calculated using Whitham's equation, Eq. (18). The pressure profile was found from the F-function as specified in NASA TN D-3082 [15], the same process as RapidF. In the following discussion and figures, the solutions from this process is referred to as the "theoretical" results.

In Fig. 19(a), the results are shown for the model with $C_L = 0$ at 10 body lengths. The pressure and distance are non-dimensionalized as:

$$\Delta \tilde{p} = \frac{\Delta p}{p_\infty} \left(\frac{h}{\mathcal{L}} \right)^{3/4}$$

$$\tilde{x} = \frac{x}{\mathcal{L}} \left(\frac{h}{\mathcal{L}} \right)^{-1/4}$$

In general RapidF agrees very well with both NASA TM X-1236's experimental and theoretical results. In fact RapidF does a better job capturing the small disturbance at $\tilde{x} = 0.1$ and the wing's overpressure from $\tilde{x} = 0.2$ to 0.4. Both NASA's theoretical approximation and RapidF have some errors associated with the nacelles from $\tilde{x} = 0.4$ to 0.6. The authors of NASA TM X-1236 were concerned about this disagreement and noted that a correction needed to be added to account for the soldering around the engines. However, this adjustment did not fully account for the difference.

Pressure profiles are presented for $C_L = 0.1$ at 10 body lengths, with and without engine nacelles, in Figs. 19(b) and 19(c), respectfully. In both graphs, RapidF properly captures the wing's overpressure, demonstrating that RapidF properly accounts for lift. The inlet shocks in Fig. 19(b) are good indicators on how well the software predicts the effects from smaller components. The difference between RapidF and the experimental results is minor compared to Carlson's theoretical pressure profile. Carlson performed the tests without nacelles because he speculated that the nacelles were causing problems. However, as can be seen in Fig. 19(c), even without the engine nacelles, Carlson's theoretical results poorly predict the pressure profile at the rear of the signature. RapidF does a better job, despite the exclusion of the wing-fuselage fillet.

Results for propagation angles of $45°$ and $180°$ at 10 body lengths can be seen in Figs. 19(d) and 19(e). For $45°$, the agreement is very good despite the fact that RapidF models the engines as one nacelle on the centerline. Examining the pressures for $180°$ in Fig. 19(e), RapidF under-predicts the wing's contribution from $\tilde{x} = 0.2$ to 0.3 for $C_L = 0.1$. The cause of this disagreement is not known and is unexpected because for all the cases thus far, RapidF has done an equal or better job matching the experimental results than Carlson's theoretical predictions. Therefore, an error in RapidF's lift or area calculations is ruled out. Furthermore, the results for $45°$ show proper application of the trigonometry for cases where $\phi \neq 0$. The authors speculate, that the NASA report mis-reported the coefficient of lift for this case because as shown in Fig. 19(e), if RapidF's C_L is set to 0.04, then all the data is in agreement. The final test case is for Mach 2.0, at 9 body

26

lenghts can be seen in Fig. 19(f), which assesses how well RapidF accounts for Mach number changes. Like the Mach 1.41 case (Fig. 19(b)), RapidF more accurately predicts the shock locations from the nacelles than the NASA theoretical solution. Also, RapidF more accurately predicts the signal duration.

A summary of the metrics used to assess to accuracy of RapidF are summarized in Table 2. Items that exceed the 10% accuracy goal are in bold. While better agreement was desired, these results should be put in perspective. The wind tunnel model was small, 10.54 cm in length and the engine nacelles were 0.142 cm in diameter. In fact, NASA TM X-1236, was inspired by previous tests [16] which used a 2.5 cm long model. NASA TX X-1236's test were scaled up from these tests in an attempt to mitigate the issues with manufacturing, measuring forces, vibrations and quantifying the boundary layer effects of very small models. Although the 10.45 cm model was better, some of these issues still exist. For example, lift was estimated (not measured) by setting the angle of attack, because the model was too small for a force balance. The angle of attack was set based on the theoretical lift curve slope including an estimation of model deformation under test conditions with 10 psi of dynamic pressure. The authors of NASA TX X-1236 concluded, "In view of the difficulty of constructing accurate small-scale models and the difficulty of evaluating boundary-layer effects for the models, there remains some doubt whether extrapolation of wind-tunnel results (based on theory) offers any increase in accuracy of flight overpressure estimates compared with estimates based on theory alone [10]." Thus, the pressure transducer data should not be interpreted as the absolutely correct solution. Typical maximum pressure recorded in a signature was 0.035 pounds per square inch. Since only 35 data points were measured along the sonic boom, resolution is limited and the shock locations had to be interpolated to obtain the data presented in Table 2. Finally, NASA TM X-1236 only tested at a maximum of 10 body lengths away. Modified linear theory is better suited for far field predictions. Also, although RapidF used 550 points along the fuselage, the fuselage description in the NASA report only had 21 points. Therefore, RapidF had to interpolate between the data provided, and minimum improvements in results should be expected from the increased grid density. The conclusion from this case is that RapidF, using modified linear theory, is capable using a geometric description to predict the pressure profile of a wind tunnel model with various configurations, lift, Mach number and propagation angles.

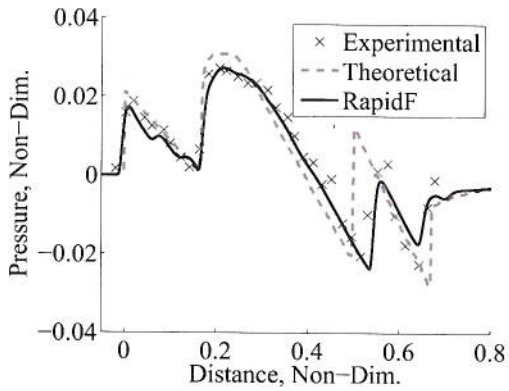**Table 2 RapidF percent difference from experimental data [10]**

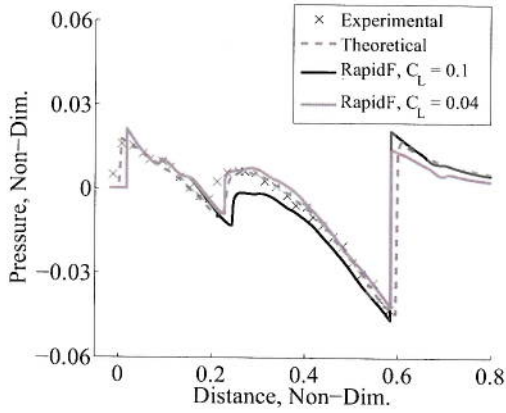| Case	Shock Loc. 1	Shock Loc. 2	Shock Loc. 3	p_{max}	p_{min}	Duration
$C_L = 0$	3.8	-4.0	N/A	**19**	**16**	-5.6
$C_L = 0.1$	3.5	-2.3	0.5	-1.4	**27**	-1.6
No engines	1.1	3.7	N/A	0.4	**-30**	-0.3
$\phi = 45^o$	-6.1	5.3	N/A	7.4	-3.3	-0.4
$\phi = 180^o$	7.8	N/A	N/A	**27**	-1.5	0.6
$M = 2.0$	**15**	-3.5	-0.8	-10	-6.7	-2.0
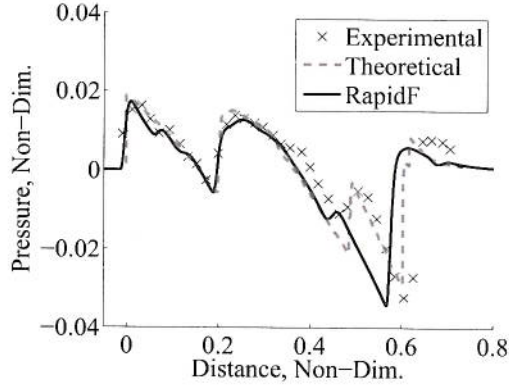
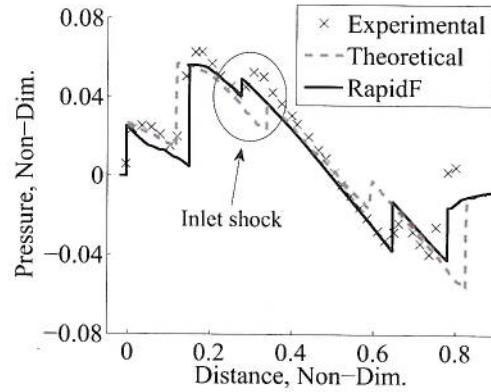(a) $M = 1.41, C_L = 0, \phi = 0.$
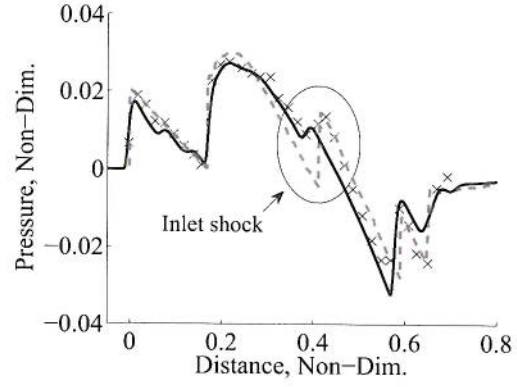
(b) $M = 1.41, C_L = 0.1, \phi = 0.$

(c) $M = 1.41, C_L = 0.1, \phi = 0,$ without nacelles.
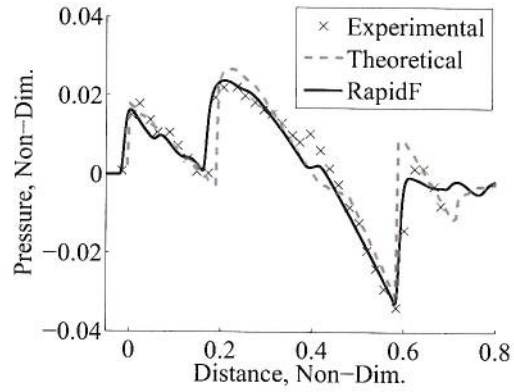
(d) $M = 1.41, C_L = 0.1, \phi = 45^o.$

(e) $M = 1.41, C_L = 0.1, \phi = 180^o.$

(f) $M = 2.0, C_L = 0.1, \phi = 0.$

Fig. 19 Pressure profiles of NASA TM X-1236 [10].

29

B. Flight Test Comparisons

1. Lockheed F-104 Starfighter

Having demonstrated the ability of RapidF to predict sonic booms in the controlled wind tunnel environment, a demonstration of its ability to replicate sonic booms from flight tests is now appropriate. In addition to the more complex flow field with winds, turbulence and humidity; replicating sonic booms from flight test is also more challenging because the test aircraft is much more complex than a wind tunnel model. An aircraft has many minor protuberances such as lights, antennas, sensors, trim tabs, etc.. Thus, in order to properly predict its sonic boom, RapidF must account for the dominate features to obtain correct area distribution and F-function.

An example of the accuracy of RapidF's cross-sectional area estimate is can be seen in Fig. 20, where the cross sectional area of an F-104 from RapidF is compared to published data [17]. It is important to note that this is the actual cross-sectional area, sliced perpendicular to the longitudinal axis, not at the Mach angle. Although there is slight differences, RapidF's area profile has the correct shape and magnitude. Thus, RapidF has enough fidelity to capture the dominant features of an aircraft.

Figure 21 compares RapidF's F-function for a 15,000 lb F-104 flying at 20,000 ft at Mach 1.4 to that published by Hayes in 1968 [18]. In order to get the lobes to line up, Hayes's F-function had to be shifted 5 ft to the left. By doing this adjustment, one can see that both F-functions have the same general shape for the
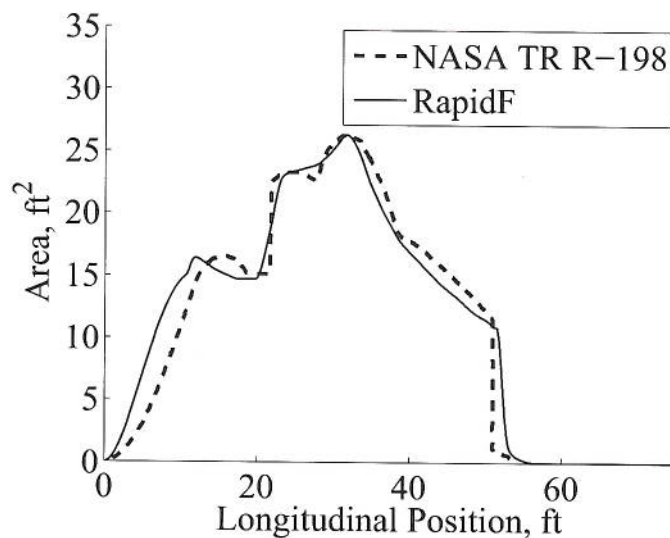

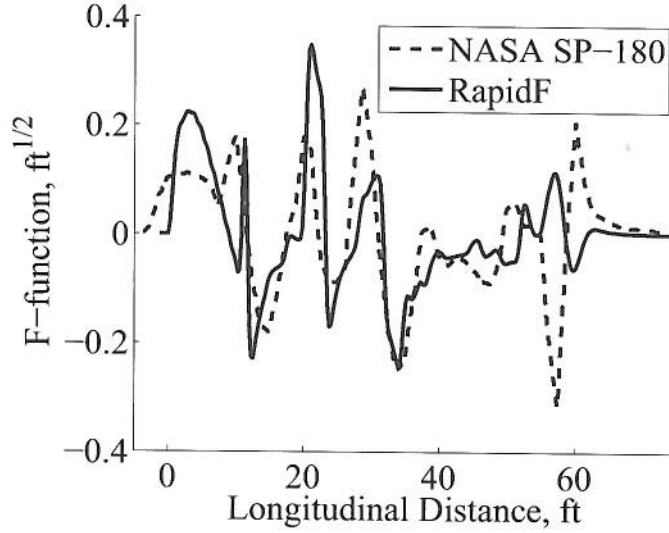**Fig. 20 F-104 cross sectional area distributions from RapidF compared to NASA TR R-198 [17].**

Fig. 21 F-functions from RapidF and NASA SP-180 for a 15,000 lb F-104 cruising at Mach 1.4 and 20,000 ft [18].

first 40 ft, but the magnitudes differ. In order to investigate these discrepancies, the F-function as presented in Eq. (4) can be inverted to find the area distribution [19]:

$$S_{eq}(y) = 4 \int_0^y F(\zeta)\sqrt{(y-\zeta)}\, d\zeta \tag{34}$$

The area determined from the above equation for Hayes's F-function is compared to that used by RapidF in Fig. 22. These results differ from the cross sectional area distribution shown in Fig. 20 in that they include lift, boundary layer growth and engine effects. They also differ in that the aircraft is cut at the Mach angle corrected for angle of attack. Both area profiles have the same shape except that Hayes's area is spread over a larger distance. The effective length of the aircraft was calculated to determine which area distribution is correct. The component that is farthest aft on the F-104 is the horizontal tail, which terminates at 54.8 ft [20] as shown in Fig. 23. Since the horizontal tail is 7.2 ft above the centerline, its influence will affect the area distribution until 61.9 ft. Thus, the effective length of the F-104 is 61.9 ft and after this location the area should remain constant. A vertical line is drawn at this location in Fig. 22. Since Hayes's area distribution continues to change past this location, it is concluded that there must be an error in his area profile. As another check, using the same process, the canopy's influence should be a maximum at 13.7 ft, yet Hayes's area distribution shows it at 20 ft. Therefore, it is concluded that our F-104 F-function is more accurate than Hayes's F-function.
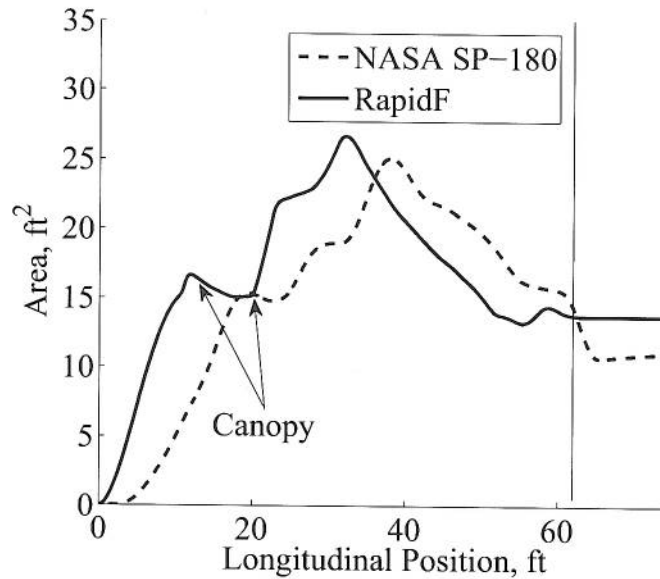
Fig. 22 F-104 equivalent area distributions from RapidF and NASA SP-180 for same case as Fig. 21 [18].

As a check of the entire RapidF system, Fig. 24(b) shows the sonic boom for an F-104 flying at Mach 1.5 and 28,000 ft compared to flight test data from NASA TN D-2539 [21]. Since only surface weather was published, RapidF used standard day conditions and no winds. Despite the limited information, RapidF properly predicted that the sonic boom is a multi-shock, saw-toothed signature. The shocks for the flight test data are considerably more smoothed out and RapidF over-predicts the peak pressures by 14% and 13%, which can be partially explained by RapidF under-predicting the effects of molecular relaxation. Additionally, like the wind-tunnel test presented earlier, the reader is reminded that the experimental data has error and is not perfect. Although the authors pf NASA TN D-2539 do not specify the uncertainty of their pressure transducers, they do state that the have a frequency response of only 5,000 Hz, which will cause shocks to be more rounded and have a lower peak pressure than reality. Thus, the differences in shock shape are of little concern. Based on this information, it can be concluded that the interior shocks are caused by the inlet and wings, respectfully. In summary, RapidF estimated the interior shock locations within 0.55% and 10%, respectfully and predicted the duration within 0.52% of the flight test results.
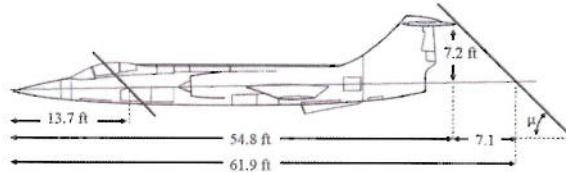
32

Fig. 23 Side view of F-104 showing influence of canopy and horizontal tail [18, 20].
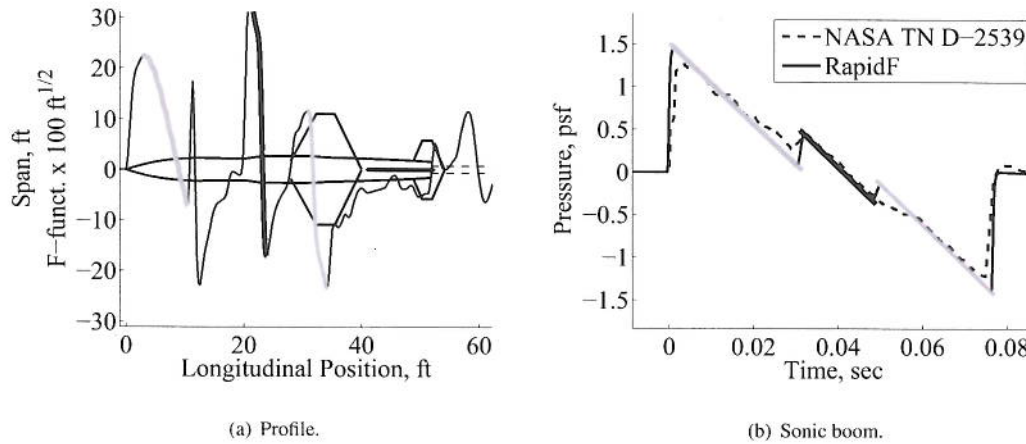

(a) Profile.

(b) Sonic boom.

Fig. 24 Sonic boom from RapidF of a F-104 flying at Mach 1.5 and 28,000 ft compared to flight test results [21].

2. Shaped Sonic Boom Demonstrator

A second example of RapidFs sonic boom prediction capability is its ability to replicate the sonic boom pressure profile from the Shaped Sonic Boom Demonstrator (SSBD), shown in Fig. 25 [22]. Figure 26 shows results for the SSBD flying at Mach 1.4 and 32,700 ft [23, 24]. For this case atmospheric data was available and entered into RapidF. The CFD solution presented was accomplished prior to flight by Lockheed-Martin using SPLITFLOW3D using an inviscid solver with 5.5 million cells. The CFD solution was propagated to the ground using PCBoom [25]. CFD predicts a weak shock at 0.02 seconds that does not exist in either of RapidF's or flight test's data. As summarized in Table 3, RapidF is nearly as accurate as the CFD–with all metrics within the 10% target, except the interior shock location. CFD under predicts this location by 55% and RapidF over predicts it by 31%. Overall, RapidF properly predicts all other metrics within 10% of the flight test results. Considering the speed of RapidF, 20 seconds on a PC for this case, and the fact that it requires no mesh generation, the slight decrease in accuracy of RapidF is an excellent trade-off for the time savings.

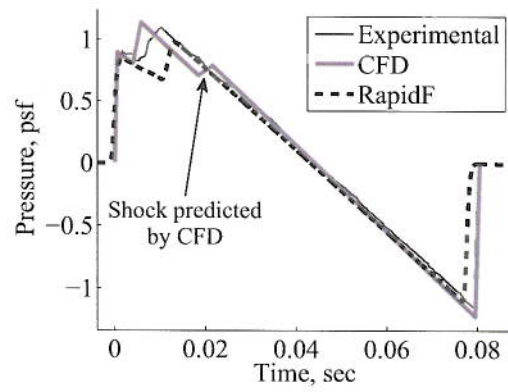**Fig. 25 SSBD (reproduced from Ref. [22]).**

Fig. 26 SSBD sonic booms for Mach 1.41 and 32,700 ft [23, 24].

In previous publications [1, 2], RapidF was unable to match the duration of the SSBD sonic boom. Fig. 27 shows the pressure profiles from Refs. [1, 2]. At the time of publishing these papers, RapidF used Lighthill's F-function, Eq. (28), and not the modified Lighthill's equation, Eq. (33). Furthermore, RapidF converted the total equivalent area to a radius: $R(\zeta) = \sqrt{S_{eq}(\zeta)/\pi}$. As discussed in the previous section, Lighthill's weighting double corrects area changes back to centerline, causing shorter than desired F-functions. Likewise, the radius based on total equivalent area also shortens the F-function. Another im-

Table 3 RapidF and CFD percent error compared to SSBD flight test [23, 24]

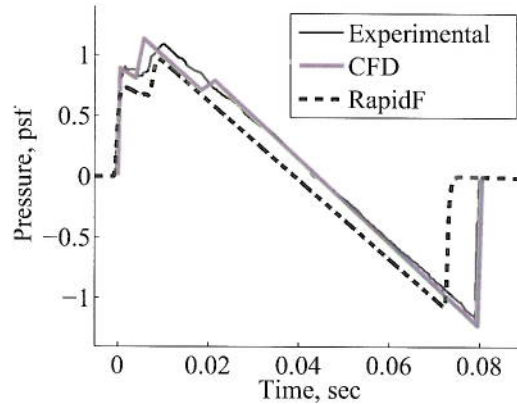|	ISPR	Shock Loc.	p_{max}	p_{min}	Duration
RapidF	-5.3	**31**	-10	-4.1	-3.7
CFD	0.11	**-55**	3.9	8.4	0.28

34

Fig. 27 Previously published [1, 2] RapidF SSBD sonic boom prediction [23, 24].

provement to CUBoom that can be seen in Fig. 26 is that the program now estimates shock rise times.

3. North American XB-70 Valkyrie

Newly refined XB-70 sonic boom data was published by Maglieri, Henderson and Tinetti in 2011 [26]. Although the testing was conducting in 1966 the data was never fully reduced to a usable form. Maglieri recognized that the data was valuable for code verification because the sonic booms were recorded in the upper atmosphere, free from the majority of the distortions created by the earth's boundary layer; thus the data was "clean." Also, the sonic booms had multiple shocks and were not simple N-waves. Furthermore, there were multiple data runs at different ranges and angles, thus allowing many comparisons. For these tests the XB-70's weight ranged from 324,000 to 350,000 lbs, the Mach number from 1.47 to 1.50 and altitude from 37,584 to 37,917 ft. The 1966 in-flight data was obtained by flying a F-104 through the sonic boom with a specially designed pressure probe. Due to the difficulty in transforming the sonic boom data to a static frame of reference, in flight sonic booms are presented with respect to a non-dimensional distance (distance / signal length). The pressure transducer used had 3% uncertainty and the reflection factor was estimated to be accurate to within 10%; yielding an overall uncertainty in the experimental data of 10.4% [26].

Images of the XB-70 can be seen in Fig. 28. RapidF's XB-70 model was made from geometric description from NASA CR-2011-217078 [27] and NASA TP 1516 [28] and can be seen in in Fig. 29. The XB-70 had several features that made inputting into RapidF difficult. First, the XB-70 had a hinged wing allowing the outer portion to deflect down during flight, as shown in Fig. 28(c). This was accounted for by projecting

35

the wing tip onto the wing horizontal plane, which appears as a wing sweep change in Fig. 29(a). The vertical projection was modeled as ventral fins, as seen in Fig. 29(b). The canard and elevator deflections were published for each test case. The canard data was inputted into RapidF, but the elevator deflections were not modeled. Instead of using a simply description of the fuselage as shown in Table 1, a radius versus distance data file was created from XB-70 drawings, which allowed a higher fidelity model of the fuselage. However, the XB-70 had a hinged nose similar to that of the Concorde. The NASA flight test data was taken with the nose in the down position; however, RapidF's fuselage model was for the nose up case. Although, the XB-70 has two inlets which distribute airflow to six engines, the engines were modeled as two large engines. The inlet capture area is published, as well as, the percent of spillage. This allowed the authors to quantify the effective area of the engine inlets. RapidF models engines as cylinders, but the XB-70's engine pod has a significant area increase as shown in Fig. 28(a). This was accounted for by adding area to the fuselage at the correct longitudinal distance (area increase can be seen in Fig. 29(a) from 120 to 170 ft). Furthermore, the inlet ducts have a system of bypasses to bleed off excessive airflow through the inlet, shown in Fig. 28(a). Although this bleed does contribute the effective cross sectional area, it was not modeled.

Sonic booms for 26 body lengths (BLs) are shown Fig. 30. Data was obtained by the F-104 as it flew 4,727 feet below the XB-70 with minimal offset ($\phi = 0.4^o$). RapidF predicts two shocks from the nose and canards separated by 30 milliseconds, matching the experiential results quite well, predicting the overpressure to within 5%. Also, by examining, Fig. 30(a), one can conclude that the two leading shocks are caused my the nose and the canards, respectfully. Looking further down the pressure profile, RapidF's solution is missing the interior shock at approximately 0.1 seconds. This missing shock was determined to be caused by RapidF under-predicting the effects of the engine inlets, as shown in Fig. 30(a). This was rectified by increasing the percent spillage from the published 38% to 99%. The results from this modification is shown on Fig. 31. This example demonstrates the power of RapidF. By examining the F-function overlaid on the aircraft (Fig. 30(a)) and correlating portions of the pressure profile with aircraft components, the cause of the discrepancy was quite intuitive.

Figure 32 shows sonic boom pressure profiles for an off-axis case with a propagation angle is 57°. The pressures were obtained 2,850 feet below and 2,900 feet to the side of the XB-70. Agian, RapidF used 99% spillage. This example is more technically challenging than the previous example because it is closer to the
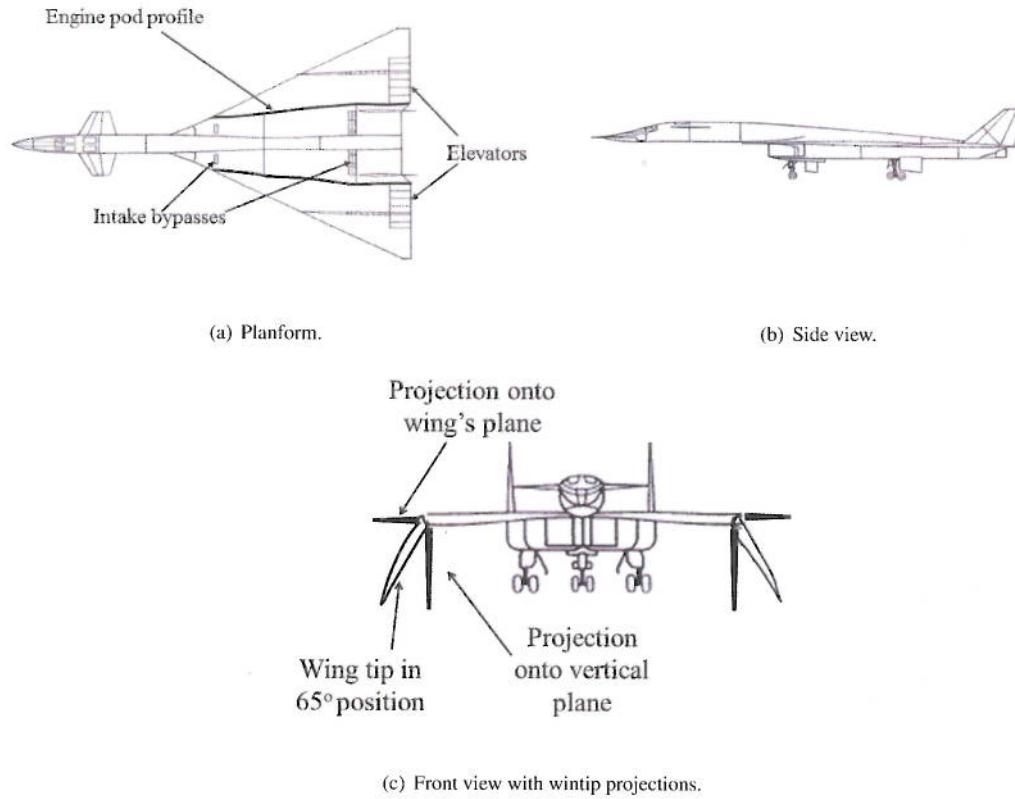
(a) Planform.

(b) Side view.

(c) Front view with wintip projections.

Fig. 28 XB-70 drawings, reproduced from Ref. [26].

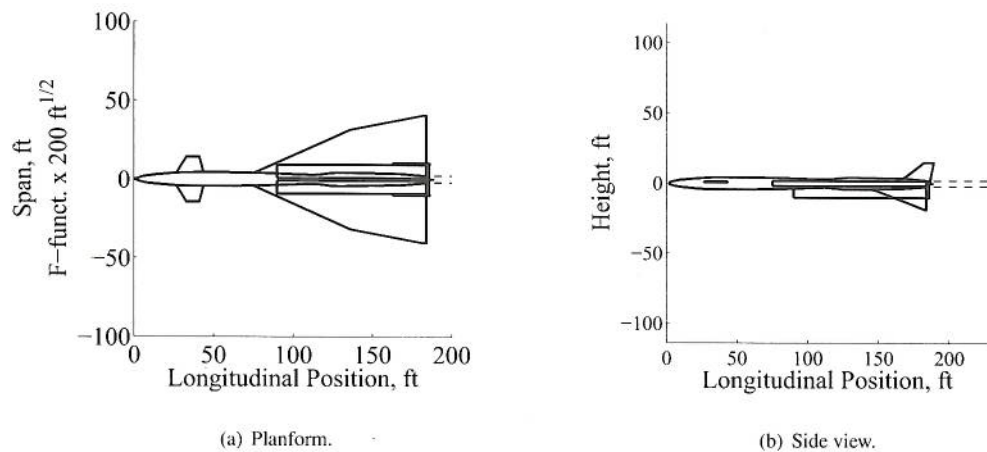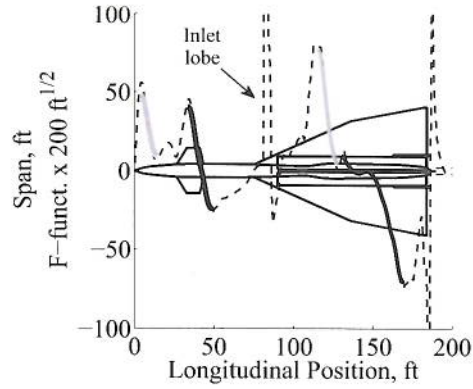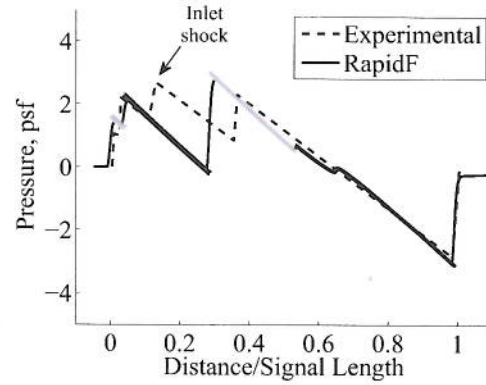(a) Planform.

(b) Side view.

Fig. 29 RapidF XB-70 model.

aircraft, 19 BLs; thus, the pressure profile is more complex. RapidF properly predicts the shock locations and magnitudes, except for the trailing shock which is over-predicted by 43%.

An over-the-top case is presented in Fig. 33. In this case the F-104 flew 3,290 feet above and 7,100 feet to the side of the XB-70, for a propagation angle of 114°. In Fig. 33(a), the pressure profile is shown for
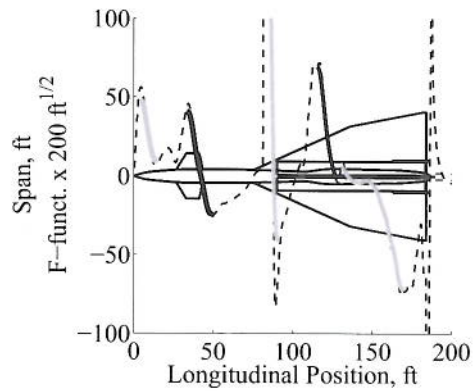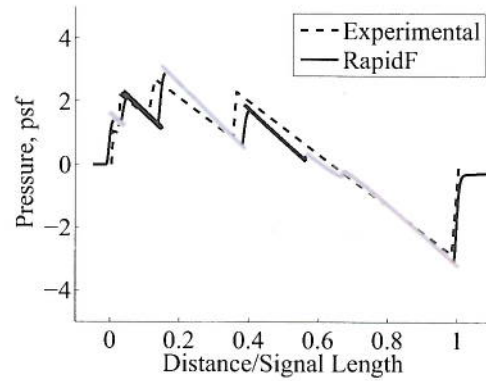
(a) Planform and F-function.

(b) Sonic boom.

Fig. 30 Sonic booms for XB-70 at 26 body lengths [26].

(a) Planform and F-function.

(b) Sonic boom.

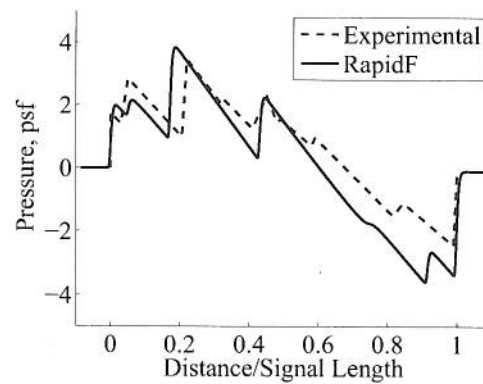**Fig. 31 Sonic booms for XB-70 at 26 body lengths with 99% Spillage [26].**

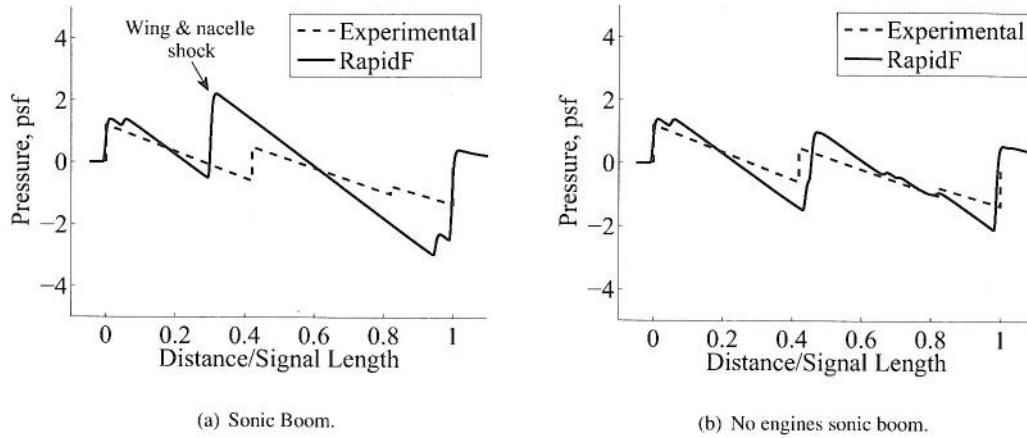

Fig. 32 XB-70 sonic boom for $\phi = 57$ and 19 BLs [26].

38

(a) Sonic Boom.   (b) No engines sonic boom.

Fig. 33 Over-the-top sonic boom for XB-70 at 42 body lengths, $\phi = 115^o$ [26].

(a) Example of slicing from above.   (b) Engines placed above wings.
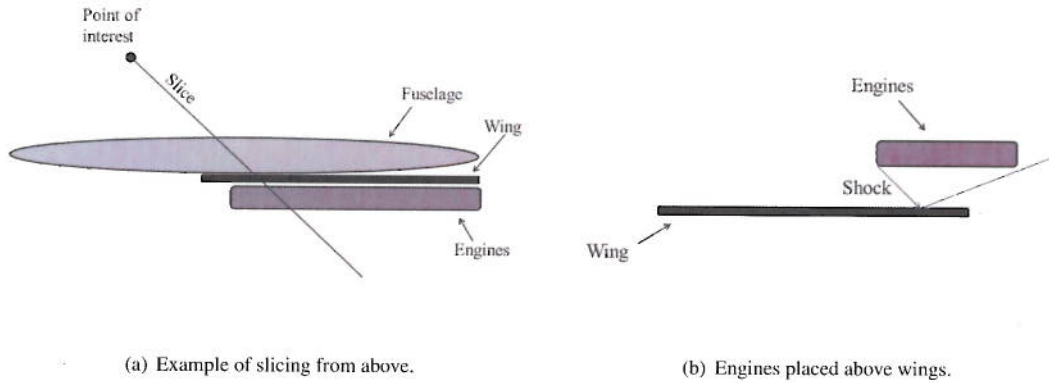
Fig. 34 Wing shielding engines.

the standard RapidF XB-70 model. The interior shock caused by the wings and inlets is over-predicted by

173%. This is because when RapidF slices the aircraft along Mach lines, it includes the fuselage, wings and

engines, as shown in Fig. 34(a). Thus, the engine inlets should contribute significantly to the sonic boom.

However, the wing serves as a barrier or shield. This prevents the engine from contributing to the sonic

boom when the engine is in the shadow of the wing. This concept has been used in reverse as a sonic boom

minimization strategy. In order to reduce the sonic boom on the ground, the engines are mounted over the

wings [29, 30]. This configuration allows the downward inlet shocks to be reflected upward by the wings, as

shown in Fig. 34(b). Thus, in order to improve the accuracy of the RapidF pressure profile, for over-the-top

sonic booms, the engine is omitted from the input, with much improved results as shown in Fig. 33(b).

Finally, the ground pressure profiles are shown in Figs. 35. Pressure data was taken from arrays of

microphones. Each array had six microphones. The accuracy of the system was estimated to be 11% by
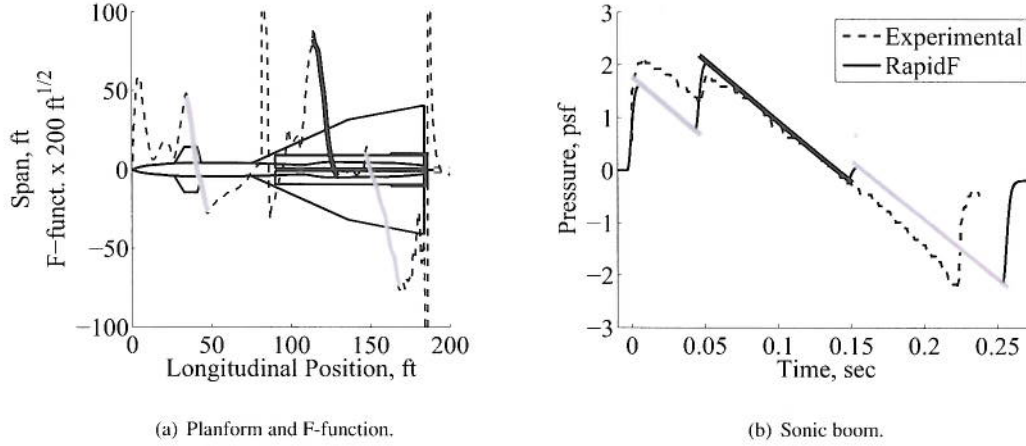
(a) Planform and F-function.

(b) Sonic boom.

Fig. 35 Sonic booms for XB-70 at the ground, 185 body lengths [26].

comparing data from all arrays. Since the ground measurements did not have the issues with a moving reference frame, the results in Figs. 35 are presented with a dimensional horizontal axis of seconds. RapidF properly predicts the shock locations and magnitude. However, it over predicts the duration by 15%. For this example, RapidF used the published XB-70 inlet spillage values. Since the spillage only needed to be modified for the data taken from 19 to 26 BLs, the authors conclude that RapidF's simple engine model is sufficiently accurate for far field sonic boom pressure profile predicts.

The results for all XB-70 cases are summarized in Table 4. The most significant errors are for the minimum pressure on the off axis cases. Since RapidF was able to properly replicate the trailing shock for all previous examples, to include off axis cases such as Fig. 19(d); the authors conclude that these large errors are unique to the XB-70 and are probably due to the abrupt termination of all components (wings, fuselage, engines and vertical tails) at 189 feet, as shown in Fig. 28. Although some other metrics exceed the 10% target, since the accuracy of the experimental data is on the order of 10%, these differences are not significant. The overall success of RapidF predicting the pressure profiles for a complex aircraft like the XB-70 indicates its reliability. Despite the fact that RapidF did not model the XB-70's nose, ailerons, and bleed air system. RapidF did model the dominate features of the aircraft which enabled it to replicate the flight test data.

IV.   Conclusions

The intent of this paper was to demonstrate the accuracy of RapidF to replicate historical sonic booms, so that the user can trust the software to predict the sonic boom of his design. RapidF is successful at this task

Table 4 Percent error of RapidF compared to XB-70 flight test [26]

Case	Shock Loc.1	Shock Loc. 2	Shock Loc. 3	p_{max}	p_{min}	Duration
$BL = 26, \phi = 0.4^o, Sp = 99\%$	-7.2	**15**	-	9.6	4.9	-
$BL = 19, \phi = 57^o, Sp = 99\%$	**-17**	0.6	-8.7	**16**	**43**	-
$BL = 189, \phi = 0^o, Sp = 38\%$	-1.5	-	-	-3.3	-1.9	**15**
$BL = 42, \phi = 115^o, Sp = 0\%$	6.6	-3.3	-	**16**	**61**	-

because it uses Lighthill's F-function equation which was shown to be superior to that of Whitham, because it converges as grid density increases and because it can accommodate discontinuities in area profiles. The weighting in Lighthill's equation was modified since RapidF already corrects for thickness when it slices the aircraft to obtain an axi-symmetric area profile. RapidF, based on modified linear theory, was able to predict sonic boom pressure profiles for wind tunnel an flight tests. However, the XB-70's complicated geometry, unique nacelle design and the bleed air made it difficult to predict its sonic boom. Despite these challenges, it was able to predict the correct shape and duration for multiple cases. In general, RapidF and modified linear theory are capable of producing a first-order pressure profile, as long as the aircraft model can be resolved into an axi-symmetric area profile. With run times less than a minute, it is ideal for preliminary design.

References

[1] Jung, T. P., Starkey, R. P., and Argrow, B., "Lobe Balancing Design Method to Create Frozen Sonic Booms Using Aircraft Components," *Journal of Aircraft*, Vol. 49, No. 6, 2012, pp. 1878–1893.

[2] Jung, T. P., Starkey, R. P., and Argrow, B., "Methodology for Conducting Scaled Sonic-Boom Flight Tests Using Unmanned Aircraft Systems," *Journal of Aircraft*, Vol. 49, No. 5, 2012, pp. 1234–1244.

[3] Jung, T. P., *Modified Linear Theory Aircraft Design Tools and Sonic Boom Minimization Strategy Applied to Signature Freezing via F-function Lobe Balancing*, Ph.D. thesis, University of Colorado, August 2012.

[4] Liepmann, H. W. and Roshko, A., *Elements of Gasdynamics*, Galcit Aeronautical Series, John Wiley & Sons, New York, 1957, pp. 178–247.

[5] Ritzel, D. V. and Gottlieb, J. J., "The Overpressure Signature from a Supersonic Projectile," Tech. Rep. UTIAS No. 279, Canadian Defense Research Establishment, 1987.

[6] Anderson, J. D. Jr., *Modern Compressible Flow: with Historical Perspectives*, chap. 8-9, McGraw-Hill, New York, 3rd ed., 2003.

[7] Whitham, G. B., "The Flow Pattern of a Supersonic Projectile," *Communications in Pure Applied Math*, Vol. 5, No. 3, 1952, pp. 301–348.

[8] Whitham, G. B., "On the propagation of weak shock waves," *Journal of Fluid Mechanics*, Vol. 1, No. 3, 1956, pp. 290–318.

[9] Walkden, F., "The Shock Pattern of a Wing-Body Combination," *Aeronautical Quarterly*, Vol. 9, No. 2, May 1958, pp. 164–194.

[10] Carlson, H. W., McLean, F. E., and Shrout, B. L., "A Wind Tunnel Study of Sonic-Boom Characteristics for Basic and Modified Models for a Supersonic Transport Configuration," *NASA TM X-1236*, May 1966.

[11] Dresher, M., *The Mathematics of Games of Strategy: Theory and Applications*, Dover, 1981.

[12] Lighthill, M. J., "Supersonic Flow Past Slender Bodies of Revolution the Slope of Whose Meridian Section is Discontinuous," *The Quarterly Journal of Mechanics and Applied Math*, Vol. 1, No. 1, 1948, pp. 90–102.

[13] Gottlieb, J. J. and Ritzel, D. V., "Analytical Study of Sonic Boom From Supersonic Projectiles," *Progresses in Aerospace Sciences*, Vol. 25, 1988, pp. 131–188.

[14] Harris, R. V.,Jr., "An Analysis and Correlation of Aircraft Wave Drag," *NASA TM X-947*, March 1964.

[15] Middleton, W. D. and Carlson, H. W., "A Numerical Method for Calculating Near-Field Sonic-Boom Pressure Signatures," *NASA TN D-3082*, November 1965.

[16] Carlson, H. W., "Correlation of Sonic-Boom Theory with Wind-Tunnel and Flight Measurements," *NASA-TR-R-213*, December 1964.

[17] H. H. Hubbard, D. J. M. V. H. and Hilton, D. A., "Ground Measurements of Sonic-Boom Pressures for the Altitude Range of 10,000 to 75,000 Feet," *NASA TR R-198*, March 1964.

[18] Hayes, W. D. and Haefeli, R. C., "The ARAP Sonic Boom Computer Code," *NASA SP-180*, edited by I. A. Schwartz, Second Conference on Sonic Boom Research, May 1968, pp. 151–158.

[19] Darden, C. M., "Sonic Boom Minimization with Nose-Bluntness Relaxation," *NASA TN-1348*, January 1979.

[20] Friend, E. L. and Sefic, W. J., "Flight Measurements of Buffet Characteristics of the F-104 Airplane for Selected Wing-Flap Deflections," *NASA TN D-6943*, August 1972.

[21] Hilton, D. A., Huckel, V., Steiner, R., and Maglieri, D. J., "Sonic-Boom Exposures During FAA Community-Response Studies over a 6-Month Period in the Oklahoma City Area," *NASA TN D-2539*, December 1964.

[22] Pawlowski, J. W., Graham, D. H., Boccadoro, C. H., Coen, P. G., and Maglieri, D. J., "Origins and Overview of the Shaped Sonic Boom Demonstration Program," *AIAA 2005-5*, January 2005.

[23] Kandel, O. A., Ozcer, I. A., Zheng, X., and Bobbitt, P. J., "Comparison of Full-Potential Propagation-Code Computations with F-5E "Shaped Sonic Boom Experiment" Program," *AIAA Paper 2005-0013*, 2005.

[24] Morgenstern, J. M., Arslan, A., Lyman, V., and Vadyak, J., "F-5 Shaped Sonic Boom Demonstrator: Persistence of

Boom Shaping Reduction through Turbulence," *AIAA Paper 2005-12*, Jan. 2005.

[25] Plotkin,K. J. and Grandi, F., "Computer Models for Sonic Boom Analysis: CABoom, BooMap, CORBoom," *Wyle Report WR 02-11*, June 2002.

[26] Maglieri, D. J., Henderson, H. R., and Tinetti, A. F., "Measured Sonic Boom Signatures Above and Below the XB-70 Airplane Flying at Mach 1.5 and 37,000 Feet," *NASA CR-2011-217077*, April 2011.

[27] Tinetti, A. F., Maglieri, D. J., and Bobbitt, P. J., "Equivalent Longitudinal Area Distributions of the B-58 and XB-70-1 Airplanes for Use in Wave Drag and Sonic Boom Calculations," *NASA CR-2011-217078*, March 2011.

[28] Arnaiz, H. H., Peterson, J. B. J., and Daugherty, J. C., "Wind-Tunnel/Flight Correlation Study of Aerodynamic Characteristics of Large Flexible Supersonic Airplane (XB-70-1) Part III," *NASA TP 1516*, March 1980.

[29] Howe, D., "Engine Placement for Sonic Boom Mitigation," *AIAA Paper 2002-0148*, January 2002.

[30] T. R. Conners, D. C. H., "Supersonic Inlet Shaping for Dramatic Reductions in Drag and Sonic Boom Strength," *AIAA Paper 2006-0030*, January 2006.